Vol. 719: 41–63, 2023
https://doi.org/10.3354/meps14393

MARINE ECOLOGY PROGRESS SERIES
Mar Ecol Prog Ser

Published September 21

Phytoplankton transport out of the euphotic zone by frontal subduction and gravitational sinking in the Santa Barbara Channel, CA, USA

Libe Washburn[1,2,*], Mark A. Brzezinski[1,3], Chris Gotschalk[1,#], Kyle Mylonakis[4], Carlos Garcia-Cervera[5], Li Kui[1]

[1]Marine Science Institute, University of California, Santa Barbara, CA 93106-6150, USA
[2]Department of Geography, University of California, Santa Barbara, CA 93106-6150, USA
[3]Department of Ecology, Evolution, and Marine Biology, University of California, Santa Barbara, CA 93106-6150, USA
[4]Protopia AI, 600 Congress Avenue, Austin, TX 78701, USA
[5]Department of Mathematics, University of California, Santa Barbara, CA 93106-6150, USA

ABSTRACT: Production of particulate organic carbon (POC) in nutrient-rich coastal waters over continental shelves, its export to depth, and its transport to deeper ocean waters is a poorly quantified component of the global carbon cycle. A critical step in quantifying this vertical transport is identifying shelf processes that export phytoplankton out of the euphotic zone. During cruises of the Santa Barbara Coastal Long Term Ecological Research project, we discovered substantial chlorophyll *a* (chl *a*) below the euphotic zone in the Santa Barbara Channel, a part of the southern California Current System. Observations from towed, undulating vehicles revealed deep chlorophyll layers near fronts where upwelled waters from central California converged with lower-density waters from the Southern California Bight. The mean fraction ± 1 standard deviation (SD) of chlorophyll biomass below the euphotic zone spanning the entire Santa Barbara Channel was ~7 ± 9% during 13 cruises averaged across all seasons. In one spring cruise, the fraction was ~30%, and in other cruises the layers were absent. Phytoplankton export out of the euphotic zone by subduction was indicated by spatial coherence between chl *a* and sloping density surfaces. Vertical plumes of chl *a* crossing density surfaces indicated enhanced gravitational export within cyclonic eddies. Chl *a* in water samples below the euphotic zone, away from fronts and cyclonic flows, suggested additional phytoplankton export. Our results emphasize the importance of subduction in the export of phytoplankton and POC out of the euphotic zone in coastal upwelling systems.

KEY WORDS: Fronts · Subduction · Flux · Particulate organic carbon · Phytoplankton · Sinking particles · POC · Chlorophyll

1. INTRODUCTION

The export to depth of particulate organic carbon (POC) from near-surface ocean waters in the euphotic zone (EZ) is a primary component of the global carbon cycle. Much of this export results from gravitational particle sinking, although recent research has revealed other export processes referred to as particle-injection pumps (Boyd et al. 2019, Buesseler et al. 2020). These pumps result from biological processes such as feeding and excretion by vertical migrators and from physical processes such as water-mass subduction (Stukel et al. 2017, Bourne et al. 2021). Much of the global production of

---

*Corresponding author: libe.washburn@ucsb.edu
[#] Retired

Publisher: Inter-Research · www.int-res.com

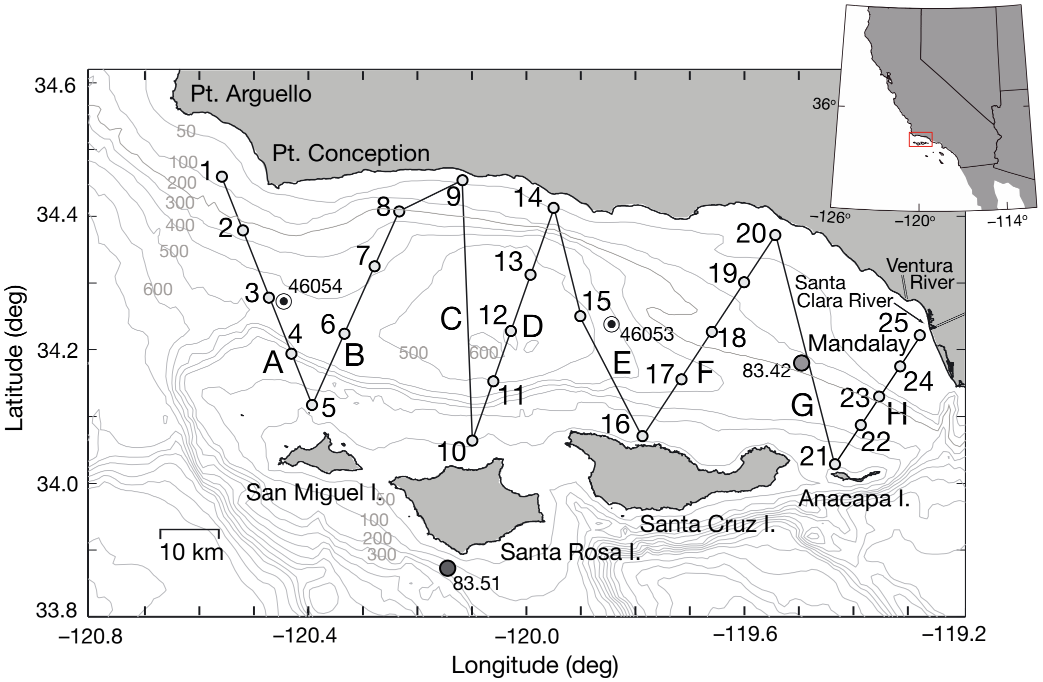

Fig. 1. Study area in the Santa Barbara Channel, California, USA. Inset shows study area (red rectangle) in relation to west coast of the USA. Cruise track (solid black line) is divided into lines labeled A–H. Light gray circles: locations of conductivity-temperature-depth (CTD)/rosette casts numbered 1–25; dark gray circles: California Cooperative Oceanic Fisheries Investigations (CalCOFI) Stns 83.51 and 83.42; circles with black dots in centers: National Data Buoy Center buoys 46054 and 46053; gray lines: bathymetric contours (m)

POC associated with phytoplankton occurs in coastal waters over continental shelves. Although they comprise about 7–10 % of ocean area, continental shelves account for about 30 % of primary productivity in the ocean (Fennel et al. 2019). Understanding the fate of POC in coastal waters and the various processes involved in its transfer to the deep ocean is critical for advancing knowledge of the global ocean carbon cycle.

In this study, we examined 2 vertical transport processes of POC in the form of phytoplankton, namely subduction and gravitational sinking, over a segment of continental shelf within the California Current System (CCS), the highly productive eastern boundary current of the North Pacific Gyre (Hickey 1979, 1998, Checkley & Barth 2009). During spring and summer, strong upwelling winds lead to high phytoplankton primary productivity in coastal waters of the CCS. These winds are driven by a combination of the North Pacific high-pressure system and the thermal low-pressure system over the deserts in western North America (Dorman & Winant 2000). The CCS transports POC from the continental shelf to the offshore North Pacific Ocean through several pathways including coastal jets, upwelling filaments, and mesoscale eddies.

Winds and phytoplankton primary productivity (hereafter productivity) are strongest along the central and northern parts of the CCS and weaken to the south in the Southern California Bight (SCB), a coastal ocean environment extending about 500 km from Point (Pt.) Conception, California, USA, to Punta Banda, Mexico. The SCB extends seaward to include the offshore Northern and Southern Channel Islands. It is unique in the CCS because it is not directly exposed to the strong equatorward winds that drive coastal circulation in the CCS north of Pt. Conception (Hickey 1993). The SCB supports highly productive habitats including reefs, kelp forests, eelgrass beds, and estuaries that support large fish, invertebrate, bird, and marine mammal populations (Schiff et al. 2016).

At the northern end of the SCB around Pt. Conception, the coastline rotates from a north–south to an east–west orientation, forming the mainland boundary of the Santa Barbara Channel (SBC, Fig. 1), our study area. As winds flow around Pt. Conception, they accelerate to speeds commonly exceeding 10 m s^{-1} in the western entrance of the SBC (Caldwell et al. 1986, Dorman & Winant 2000). These strong winds stimulate high productivity in an upwelling center at Pt. Conception, and some of the phytoplankton produced there advects eastward into the SBC along the Northern Channel Islands (Otero & Siegel 2004, Brzezinski & Washburn 2011). In regions farther east in the SBC, weaker winds prevail due to sheltering by coastal mountains extending eastward from Pt. Conception.

Currents in the SCB and the SBC result from prevailing equatorward winds and poleward pressure gradients set up by the large-scale wind field (Lynn & Simpson 1987, Harms & Winant 1998). Currents west of Pt. Conception and west of the SCB are equatorward, consistent with flow in the CCS. Within the SCB, the prevailing flow is generally weaker and poleward due to the Southern California Counter Current (Hickey 1979, Lynn & Simpson 1987, Bray et al. 1999). This warm northward flow spreads westward south of the Northern Channel Islands and enters the SBC through its eastern entrance. Colder, upwelled, and equatorward-flowing waters often enter the SBC through its western entrance and encounter the warmer waters of the Southern California Counter Current entering from the east. This forms strong temperature and density fronts within the SBC and along the northern coasts of the Northern Channel Islands (Selkoe et al. 2006). Equatorward flow can also occur in the SCB during spring due to strong equatorward winds (Lynn & Simpson 1987, Harms & Winant 1998, Bray et al. 1999).

Productivity within the SBC exceeds levels found elsewhere in the SCB (Mantyla et al. 1995), especially in spring. Currents in the SBC shape the spatial patterns of this high productivity (Otero & Siegel 2004, Brzezinski & Washburn 2011). These currents are largely described by 3 patterns (Harms & Winant 1998, Winant et al. 2003): (1) the upwelling pattern with prevailing equatorward flow except near the mainland coast where the flow is poleward; (2) the convergent pattern with equatorward flow north of Pt. Conception and poleward flow east of Pt. Conception such that currents converge near Pts. Conception and Arguello; and (3) the relaxation pattern with poleward flow over much of the channel. Cyclonic flow in the western channel frequently occurs and often closes to form eddies that can span the channel (Harms & Winant 1998, Oey et al. 2001, Nishimoto & Washburn 2002, Winant et al. 2003, Beckenbach & Washburn 2004).

The upwelling and cyclonic flow patterns lead to high productivity within the SBC, and the relaxation pattern leads to lower productivity (Brzezinski & Washburn 2011). The productivity effects of the convergent pattern are not known, but are probably small or highly variable since the upwelling and cyclonic eddy patterns together account for about 80 % of the patterns of spatial and temporal productivity variance (Brzezinski & Washburn 2011). The distributions of surface chlorophyll *a* (chl *a*) concentration from satellite imagery shift according to the spatial patterns of currents in the channel (Otero & Siegel 2004, Anderson et al. 2006, 2009). Some of this productivity leads to harmful algal blooms that cause extensive mortality in sea birds and marine mammals. This occurred during 1 of the cruises discussed below (cruise 7) when a large, toxic bloom of the diatom *Pseudo-nitzschia australis* was present in the SBC (Anderson et al. 2006). Closer to shore, high productivity in the channel is supported by nutrients transported to shallow water by processes including the internal tide (McPhee-Shaw et al. 2007, Fram et al. 2008, Lucas et al. 2011a,b) and nearshore eddies (Bassin et al. 2005). Intermittent storm water runoff plumes during winter and spring also deliver nutrients to nearshore waters that can stimulate productivity (McPhee-Shaw et al. 2007, Fram et al. 2008).

The transport and fate of productivity in the SBC is not well established, but some pathways have been identified. Sediment trap studies indicate that POC exported by gravitational sinking to the 600 m deep Santa Barbara Basin in the western SBC derives mainly from marine phytoplankton with much of the productivity and export occurring during spring diatom blooms (Thunell et al. 1995, Thunell 1998, Shipe & Brzezinski 2001, Shipe et al. 2002, Sekula-Wood et al. 2011, 2012). After sinking to the seafloor, this material is incorporated into varved sediments characteristic of the basin (Soutar & Crill 1977, Soutar et al. 1977). Another pathway is advective transport from offshore to the inner shelf where phytoplankton constitute an important subsidy to near-shore, benthic marine communities (Miller et al. 2011, Goodman et al. 2012). In our analysis of data obtained from cruises as part of the Santa Barbara Coastal Long Term Ecological Research (SBC LTER) project, we discovered that a third process operated in the SBC, namely subduction of phytoplankton along sloping density surfaces within fronts between water masses.

Transport of phytoplankton and POC from near surface waters by subduction has been found in previous studies of the CCS (Hood et al. 1991, Kadko et al. 1991, Washburn et al. 1991, Murphy & Cowles 1997, Flament & Armi 2000). More recently, Evans et al. (2015) described evidence for subduction off the Oregon (USA) coast based on ocean glider-based observations of chl *a* fluorescence. Stukel et al. (2017, 2018) used data-assimilative models combined with *in situ* observations to estimate the enhanced flux of POC resulting from subduction at fronts in the southern CCS. These observations were conducted during cruises of the California Current Ecosystem LTER project. These studies, along with that of Bourne et al. (2021) in and around an upwelling filament off Pt. Conception, found that remineralization confined the subducted POC flux to depths above 150 m. They also found that larger particles such as fecal pellets reached greater depths before remineralization.

Many details of the physical processes that transport phytoplankton vertically out of the EZ in coastal waters are unclear and several questions remain. How do density fronts lead to subduction of phytoplankton and POC? What is the relative importance of subduction versus gravitational sinking in the vertical transport of phytoplankton? How do eddies affect phytoplankton sinking and subduction? Does the presence of islands contribute to subduction? In this paper, we address these questions based on high-resolution sections of chl *a* fluorescence, temperature, salinity, and density obtained from towed profilers and horizontal currents obtained from underway, shipboard observations. The paper is organized as follows. Section 2 summarizes the cruises, shipboard observations, ancillary data sources, and analysis methods. Section 3 describes the results, including estimates of phytoplankton biomass below the EZ and evidence of downward phytoplankton transport by subduction and gravitational sinking. Section 4 discusses photoadaptation effects, productivity rates below the EZ, and particle sinking versus subduction due to eddies and other processes.

2. MATERIALS AND METHODS

2.1. Summary of cruises

A total of 16 seasonal cruises were conducted during 2001 to 2006 in the SBC from the RV 'Point Sur.' An observational goal of the cruises was to map offshore chl *a*, water mass, and productivity distributions in the SBC during the 3 main seasons: spring upwelling, the fall oligotrophic period, and winter when storms occur. Winter cruises (January through March) were timed to observe low productivity; spring cruises (April and May) were timed to observe highly productive upwelling conditions; and fall cruises (September and October) were timed to observe stratified, oligotrophic conditions.

During the cruises, a conductivity-temperature-depth (CTD)/rosette system collected water column data at 25 stations along 8 lines labeled A through H extending from Pt. Conception to the Ventura River n California (Fig. 1). The northern apex of lines B and C was shifted eastward after cruise 1 (see Fig. 17a,b). A photosynthetically available radiation (PAR) sensor (Biospherical Instruments) was mounted on the CTD/rosette system (SeaBird 911 CTD) to measure the subsurface light field. A second PAR sensor was mounted on the ship's mast to obtain incident PAR at the sea surface. The rosette carried 12 l Niskin bottles to obtain seawater samples for nutrients, chl *a*, POC, and other water properties. Brzezinski & Washburn (2011) described the methods for measuring concentrations of nutrients and chl *a*, and primary productivity. POC concentrations were measured in 630 ml water samples filtered through pre-combusted glass fiber filters and analyzed with a Leeman Labs (Model 440) carbon–hydrogen–nitrogen analyzer. Samples were collected at 7 depths from the surface to 75 m, although a few bottle samples were missed. Primary productivity at 5 m depth was measured at the 25 stations during 15 of the 16 cruises. Profiles of primary productivity within the EZ, defined as the depth interval from the surface down to the 1% light depth, were obtained along a transect of 7 stations across the middle of the Channel (locations shown by Brzezinski & Washburn 2011).

During cruises 1, 4, and 7 reported here, vertical profiles of current velocity components u and v (positive eastward and northward, respectively) were obtained to depths up to 370 m in 8 m bins from a vessel-mounted, acoustic Doppler current profiler (ADCP, Teledyne RD Instruments) operating at 150 kHz. Velocity data from the ADCP consistently extended below 100 m, but were not available above 24 m depth. Very limited ADCP data were available during cruise 13 and are not reported here. This analysis centers on observations from towed profiler surveys in the upper 100 m that were collected before and after the CTD surveys discussed by Brzezinski & Washburn (2011).

Poleward wind τ stress beginning 2 d before the start and averaged through the end of each profiler survey was calculated from NOAA buoys 46011, 46023, 46053, and 46054 and are given in Table 1 as τ_{46011}, τ_{46023}, τ_{46053}, and τ_{46054}. Brzezinski & Washburn (2011) described the method for computing poleward wind stress. $\tau < 0$ indicates upwelling-favorable winds. Locations of buoys 46053 and 46054 are shown in Fig. 1; locations of 46011 (34.956° N, 121.019° W) and 46023 (34.714° N, 120.967° W) were north of the study area.

Limited observations of surface currents (upper 1 m) were available from high-frequency (HF) radars located along the coastline. Details on data processing for surface currents from the radars are given by Brzezinski & Washburn (2011).

Table 1. Summary of times and conditions for cruises with towed profiler surveys. Surveys 1 and 2 were the first and second completed surveys during cruises 2, 5, 12, 14, and 15. During some cruises, the first towed survey was incomplete, but the second survey was completed (e.g. cruise 1). During other cruises, only a single survey was attempted or the second survey was not completed. No fluorometer data were collected during cruises 3 and 6, and the profiler was lost during cruise 10. $p_{1\%}$ is pressure at the 1% light depth. Chlorophyll (chl) *a* biomass (CB) was computed using 3 methods: Eq. (1) (CB_1), ordinary kriging (CB_2), and optimal interpolation (CB_3). The fluorometer on the towed profiler fouled during survey 1 of cruise 11 so CB values were not computed. Ratios $CB_{3\text{-S1}}/CB_{3\text{-S2}}$ were computed as (CB_3 from survey 1)/(CB_3 from survey 2) for cruises 2, 5, 12, 14, and 15. Chl *a* biomass below $p_{1\%}$ was computed using the 3 methods: Eq. (1) ($CB_{1\text{-p1\%}}$), ordinary kriging ($CB_{2\text{-p1\%}}$), and optimal interpolation ($CB_{3\text{-p1\%}}$). Ratios $CB_{1\text{-p1\%}}/CB_1$, $CB_{2\text{-p1\%}}/CB_2$, and $CB_{3\text{-p1\%}}/CB_3$ were percentages of chl *a* below $p_{1\%}$ computed using the 3 methods. VC_K, VC_{OI}, and VC_C are vertically integrated chl *a* biomass ± 1 SD using ordinary kriging, optimal interpolation, and from Table 1, column 8, in Brzezinski & Washburn (2011), respectively. VC_C values are repeated for cruises with 2 surveys. τ_{46011}, τ_{46023}, τ_{46054}, and τ_{46053} were poleward wind stresses at National Data Buoy Center buoys 46011, 46023, 46054, and 46053, respectively. Wind stresses were averages from 2 d before the cruises to the end of the towed profiler surveys. Computation of poleward wind stress is explained in Brzezinski & Washburn (2011). Negative τ indicates equatorward (upwelling-favorable) wind stress. Dashes indicate missing data

Cruise	Survey	Dates	$p_{1\%}$ dbar	CB_1 10^5 kg	CB_2 10^5 kg	CB_3 10^5 kg	$CB_{3\text{-S1}}/CB_{3\text{-S2}}$	$CB_{1\text{-p1\%}}$ 10^5 kg	$CB_{2\text{-p1\%}}$ 10^5 kg	$CB_{3\text{-p1\%}}$ 10^5 kg	$CB_{1\text{-p1\%}}/CB_1$ %	$CB_{2\text{-p1\%}}/CB_2$ %	$CB_{3\text{-p1\%}}/CB_3$ %	VC_K mg m^{-2}	VC_{OI} mg m^{-2}	VC_C mg m^{-2}	τ_{46011} Pa	τ_{46023} Pa	τ_{46054} Pa	τ_{46053} Pa
1 Spring	2	25–26 Mar 2001	37	2.2	2.7	2.8	–	0.056	0.040	0.057	2.6	1.5	2.1	59±28	64±32	67±35	–0.040	–0.052	–0.12	–0.074
2 Fall	1	9–10 Sep 2001	39	1.4	1.8	2	–	0.028	0.020	0.037	1.9	1.1	1.9	41±20	49±20	73±32	–0.0016	–	–0.014	–0.022
2 Fall	2	13–Sep 2001	39	1.6	2.3	2.2	0.91	0.13	0.15	0.16	8.4	6.8	7.0	46±21	52±23	73±32	–0.042	–	–0.10	–0.034
4 Spring	1	26–27 Apr 2002	28	5.2	7.5	7.2	–	0.80	1.14	1.1	15	16	15	144±84	127±88	177±99	–0.029	–0.041	–	–0.069
5 Fall	1	5–6 Sep 2002	38	1.3	1.7	1.7	–	0.011	0.005	0.029	0.88	0.32	1.7	32±11	36±12	65±26	–0.034	–0.051	–0.12	–0.021
5 Fall	2	9–10 Sep 2002	38	1.0	1.3	1.3	1.31	0.010	0.001	0.003	1.0	0.04	0.2	25±13	31±16	65±26	–0.078	–0.081	–0.12	–0.022
7 Spring	2	19–20 May 2003	18	10	13	13	–	2.6	3.3	3.1	26	25	24	254±61	291±78	302±115	–0.13	–0.191	–0.19	–
8 Fall	1	13–15 Oct 2003	34	1.2	1.7	1.6	–	0.013	0.006	0.01	1.1	0.36	0.64	41±19	43±22	54±16	–0.053	–0.084	–0.053	0.000
9 Winter	1	1–2 Mar 2004	26	5.1	6.9	6.6	–	1.1	1.4	1.4	22	21	21	135±49	145±57	194±90	–0.068	–0.11	–0.14	–0.077
11 Fall	1	10–11 Sep 2004	47	–	–	–	–	–	–	–	–	–	–	36±23	39±24	71±37	–0.026	–0.046	–0.087	–0.015
11 Fall	2	14–15 Sep 2004	47	0.7	0.8	1.0	–	0.0012	0	0	0.18	0	0	25±14	30±18	71±37	–0.11	–0.19	–0.25	–0.025
12 Winter	1	21–22 Jan 2005	40	0.9	1.2	1.3	–	0.0087	0	0.014	1.0	0	1.1	28±13	28±15	60±22	–	–0.013	–	–0.0050
12 Winter	2	26–27 Jan 2005	40	0.2	0.3	0.3	4.33	0.0026	0	0.003	1.1	0	0.95	19±12	18±12	60±22	–	0.061	–	0.016
13 Spring	2	27–29 Apr 2005	32	6.6	9.8	11	–	1.5	2.8	3.7	22	28	35	205±56	266±68	328±209	–	–	–	–0.0033
14 Fall	1	8–9 Oct 2005	29	2.7	3.6	3.7	2.89	0.20	0.21	0.25	7.6	6.0	6.8	70±30	60±24	87±34	–0.055	–0.10	–0.17	–0.060
14 Fall	2	12–13 Oct 2005	29	2.7	3.8	4	–	0.11	0.15	0.21	4.1	3.9	5.4	75±20	70±23	87±34	–0.025	–0.041	–0.066	–0.0094
15 Winter	1	3–4 Feb 2006	36	3.1	4.3	4.1	–	0.12	0.14	0.16	4.0	3.2	3.9	87±34	82±38	90±38	–0.11	–0.14	–0.26	–0.081
15 Winter	2	7–9 Feb 2006	36	4.3	5.8	5.6	0.73	0.097	0.065	0.14	2.2	1.12	2.5	120±32	114±33	90±38	0.0012	–0.0049	–0.0068	0.0075
16 Spring	1	27–28 Apr 2006	27	4.1	5.9	5.6	–	0.36	0.53	0.48	8.8	9.0	8.5	112±37	110±43	152±42	–0.035	–0.054	–0.055	–0.055

2.2. Towed profiler surveys

We analyzed data from 13 of the cruises when towed profiler surveys were conducted. For cruises 1–7 and 14, a Scanfish MKII profiler (Geological & Marine Instrumentation) was used. For the remaining cruises, a Triaxus profiler (MacArtney Underwater Technology) was used. The profilers carried SeaBird CTD instruments, chl *a* fluorometers (WetLabs WETStar), and beam transmissometers (WetLabs C-Star, 660 nm, 0.25 m path length). No fluorometer data were collected during cruises 3 and 6, and the profiler was lost during cruise 10. The fluorometer fouled during the first profiler survey of cruise 11.

The profilers were towed at ~4 m s^{-1} (nominally 8 knots) and undulated from near the surface (0 to 5 m depth) to 100–120 m or a few meters above the seafloor in shallower water. Profiles were obtained on upcasts and downcasts, and the midpoints of profiles were about 500 m apart. We obtained 19 profiler surveys during the 13 cruises, covering a total distance of ~5800 km. During cruises 2, 5, 11, 12, 14, and 15, 2 profiler surveys were completed 2–4 d apart. During the other cruises, a single profiler survey was completed. Line A was not sampled during the profiler survey of cruise 8 and during the second survey of cruise 11; all other surveys sampled lines A–H. Table 1 summarizes the seasons and dates of the surveys.

Sensor data from the profilers were recorded at 24 Hz and then averaged over 1 s intervals to form the basic data set for analysis. The 1 s conductivity data c were delayed relative to temperature to remove systematic salinity offsets (i.e. hysteresis) between upcasts and downcasts as the profilers moved through the thermocline. The delayed conductivity c_n' at time point n was computed from c_n as $c_n' = \alpha c_n + (1 - \alpha) c_{n-1}$. For all but 2 cruises, α was in the range 0.8–0.9. For cruise 9, α was 1.0, corresponding to no delay, and for cruise 14, α was 0.35, corresponding to a longer delay, possibly due to different plumbing in the particular Scanfish used for that cruise.

2.3. EZ depth and fluorometer calibration

We used fluorescence-derived chl *a* as a dye, uniquely produced in the EZ, to trace vertical movements of water masses and phytoplankton. Chl *a* fluorescence can be mapped at spatial resolutions similar to those of temperature, salinity, density, and currents and therefore can be used to examine phytoplankton transport processes.

The base of the EZ was estimated as the pressure level ($p_{1\%}$) where the measured PAR from the sensor on the CTD/rosette dropped to 1% of its surface value as measured by the PAR sensor on the mast of the research vessel. Sub-surface PAR data were not available during the profiler surveys. Instead, PAR profiles were obtained within ±3 h of local noon during the CTD/rosette surveys that immediately preceded or followed the profiler surveys. About 9 PAR profiles per cruise were available for estimating $p_{1\%}$. The deepest $p_{1\%}$ during each cruise was taken as the base of the EZ. Table 1 shows $p_{1\%}$, which ranged from 18 to 47 dbar, for all cruises.

Chl *a* fluorescence measured on the towed profilers was calibrated to chl *a* by comparison with the bottle samples obtained in the CTD/rosette surveys. For each 25-station CTD/rosette survey, the median chl *a* profile $C_m(z_b)$ in mg m^{-3} was computed at up to 6 sampling depths z_b, depending on water depth. The surface bottle samples were not used because the profilers did not consistently sample the upper 2 m of the water column. For each profiler survey, the median fluorescence profile $F_m(z_b)$ in volts was computed from all vertical profiles at bottle depths z_b. Each value of $F_m(z_b)$ was the median of F within ±1 m of z_b. The calibration coefficients (slope and offset) for each survey were obtained by a linear least square fit between F_m and C_m; r^2 for the fits was in the range 0.44–0.98, with mean $r^2 \pm 1$ SD = 0.85 ± 0.18, $p < 0.02 \pm 0.05$. If the 2 lowest values are excluded ($r^2 = 0.44$, cruise 8; $r^2 = 0.53$, cruise 11), the mean $r^2 = 0.92 \pm 0.07$, $p < 0.005 \pm 0.007$. In this analysis, we only included fluorescence-derived chl *a* ≥ 1 mg m^{-3}. Due to a higher noise level in the fluorometer during cruise 13, a higher threshold was used, i.e. chl *a* ≥ 1.3 mg m^{-3}.

Patterns of chl *a* were consistent with other observations from the profilers and from the CTD/rosette measurements of these cruises and cruises of the California Cooperative Fisheries Investigations (CalCOFI). CalCOFI is a long-term oceanographic program to study the physics, biology, and biogeochemistry of the CCS (calcofi.org). For example, comparison of contoured sections along towed profiler lines of chl *a* and the diffuse attenuation coefficient at 660 nm derived from the transmissometer measurements showed very similar patterns to chl *a* away from the seafloor as expected when phytoplankton comprise most of the particle fields (data not shown).

2.4. Estimating chl *a* biomass

Chl *a* biomass (CB, in units of kg) in the survey volume across the entire SBC was estimated in 3 ways to test the sensitivity of CB estimates to interpolation method. For the first estimate, CB_1, chl *a* and other water property data were interpolated using ordinary kriging onto regular grids along lines A–H with a pressure interval 2 dbar and a horizontal spacing of 500 m. Depths of isopycnals along the lines interpolated from kriging closely matched isopycnal depths obtained directly from the towed CTDs (data not shown). The maximum sampling depth D was usually 100 m in deeper water and a few meters above bottom in shallower water. For each line, chl *a* was integrated vertically (1 dbar = 1 m assumed hereafter) over the profiling depth D and horizontally over the north–south length of line L to estimate the integrated chl *a* (IC) per meter in the east–west direction. For example, the contribution to CB_1 from the portion of the survey volume containing line B, was estimated as $IC_B \times \Delta x_B$, where $\Delta x_B = 0.5(x_C - x_A)$, $x_C - x_A$ is the east–west distance between midpoints of line A and line C, and x is positive eastward. This assumes the distribution of chl *a* along line B represents the distribution of chl *a* within a box-shaped portion of the survey volume with horizontal dimensions L_B by Δx_B. CB_1 over the survey volume was estimated by summing contributions to CB_1 over all lines as:

$$CB_1 = 0.5\left[\sum_{j=A}^{H} IC_j \cdot \Delta x_j\right] \quad (1)$$

where Δx_j for j = B to G is the x-distance between midpoints of lines $j + 1$ and $j - 1$. For j = A, Δx_j is the

x-distance between midpoints of lines A and B, and for j = H, Δx_j is the x-distance between midpoints of lines G and H. Chl *a* biomass below the EZ $CB_{1\text{-p}1\%}$ was estimated similarly, but with chl *a* integrated below $p_{1\%}$. CB_1 and $CB_{1\text{-p}1\%}$ values for the cruises are given in Table 1.

For the second estimate, CB_2, water properties were interpolated onto a 3-dimensional grid using ordinary kriging. Besides chl *a*, potential temperature (T), salinity (S), density (ρ), potential density anomaly (σ_θ), and u and v from the ADCPs were also interpolated onto the grid. Grid spacing was Δx = 5 km, Δy = 5 km, and Δp = 2 dbar. CB_2 was estimated by integrating chl *a* vertically and horizontally over the grid.

For the third estimate, CB_3, water properties and ADCP currents were interpolated onto the same 3-dimensional grid as for CB_2, but optimal interpolation was used instead of ordinary kriging. A Gaussian decorrelation scale of 5 km was applied in the x- and y-directions, and chl *a* biomass below the EZ $CB_{3\text{-p}1\%}$ was estimated similarly to $CB_{2\text{-p}1\%}$. Table 1 shows estimates of CB_1, $CB_{1\text{-p}1\%}$, CB_2, $CB_{2\text{-p}1\%}$, CB_3, and $CB_{3\text{-p}1\%}$. Estimates of CB_2 and CB_3 agreed closely with $r^2 = 0.994$ and $CB_2 = 0.993\ CB_3 + 0.019 \times 10^5$ kg (Fig. S1a in the Supplement at www.int-res.com/articles/suppl/m719p041_supp.pdf), indicating that the results did not strongly depend on the interpolation method. Estimates CB_1 and CB_3, though highly correlated ($r^2 = 0.984$), agreed less closely with $CB_1 = 0.713\ CB_3 + 0.040 \times 10^5$ kg (Fig. S1b), consistent with the more dissimilar estimation methods.

As a further check on the chl *a* calibration and biomass estimates, we found good agreement between mean vertically integrated chl *a* values (VC) using optimal interpolation (VC_{OI}) and using kriging (VC_K). We also found good agreement between VC_{OI} and VC from CTD casts (VC_C). Values of VC_C were obtained by Brzezinski & Washburn (2011) (see their Table 1, column 8) by integrating chl *a* vertically at each CTD station from bottle samples and then averaging over all stations for each cruise. For the towed survey grids, VC_{OI} and VC_K were estimated by first vertically integrating chl *a* at each grid point to get integrated chl *a* $VC(x_i, y_i)$, where x_i and y_i are the coordinates of the i^{th} grid point. $VC(x_i, y_i)$ values were then averaged over all grid points to get VC_{OI} and VC_K. Table 1 shows VC_{OI}, VC_K, and VC_C along with their standard deviations. VC_{OI} was highly correlated both with VC_K ($r^2 = 0.97$, Fig. S2a) and with VC_C ($r^2 = 0.94$, Fig. S2b). VC_C was biased higher than VC_{OI}, possibly due to the limited vertical resolution of the bottle sampling (Fig. S2b).

2.5. Estimating geostrophic velocity

Our zig-zag sampling pattern (Fig. 1) was designed to provide consistent, channel-wide, synoptic 'snapshots' of water properties and currents in the SBC over many cruises. To improve resolution of flow structures such as eddies and current meanders and to indicate flow paths between transect lines, we used the method described by Rudnick (1996) to compute geostrophic velocity fields that best matched the ADCP data, were non-divergent, and satisfied the thermal wind equations. The equations used are repeated below, and Rudnick (1996) more thoroughly discussed the method. We computed geostrophic velocities for cruises 4 and 7 because these cruises had the highest chl *a* biomass amounts below the EZ (Table 1) when ADCP data were available. We speculated that these cruises would provide the clearest evidence of flow structures associated with subduction and other vertical transport processes.

We experimented with various grids for computing geostrophic velocity fields. Results reported here were based on a grid in the southern part of the study area encompassing regions of high chl *a* biomass below the EZ and where strong horizontal density gradients occurred. This grid extended to $z = -100$ m, so it included all depths sampled by the profilers and exceeded the maximum depths with chl $a > 1$ mg m^{-3} below $p_{1\%}$. The grid was 39 × 12 × 50 points in the x, y, and z dimensions, respectively, with uniform horizontal spacing $\Delta x = \Delta y = 2.5$ km and vertical spacing $\Delta z = 2$ m.

The non-divergent, geostrophic velocity field that satisfies the thermal wind equation with eastward and northward velocity components u_g, v_g is:

$$u_g = -\frac{\partial \psi}{\partial y} + \frac{\partial R}{\partial y} \tag{2}$$

$$v_g = \frac{\partial \psi}{\partial x} - \frac{\partial R}{\partial x} \tag{3}$$

where R is:

$$R = \frac{g}{\rho_0 f}\int_{z_0}^{z} \rho \, dz \tag{4}$$

z is positive upward, g is the gravitational acceleration (9.81 m s^{-2}), f is the Coriolis parameter (8.175×10^{-5} s^{-1} 34.2° N), $z_0 = -100$ m, and ρ_0 is the reference density (1025 kg m^{-3}). The stream function $\psi(x, y)$ satisfies:

$$\nabla^2 \psi = \tilde{H}^{-1}\left(\nabla^2 \tilde{R} + \tilde{\zeta}\right) \tag{5}$$

with boundary conditions:

$$\boldsymbol{n} \cdot \nabla \psi = \tilde{H}^{-1}\left(\boldsymbol{n} \cdot \nabla \tilde{R} + \boldsymbol{s} \cdot \tilde{\boldsymbol{u}}\right) \tag{6}$$

such that u_g and v_g best match the ADCP velocities u, v. Here $\tilde{H} = z_A - z_O = 74$ m 74 m where $z_A = -26$ m, the shallowest depth where ADCP data were consistently available. $\boldsymbol{n}$ and $\boldsymbol{s}$ are unit vectors perpendicular (positive outward) and tangential (positive counter-clockwise) to the boundary. $\tilde{R}$ is R integrated from z_0 to z_A. $\tilde{\boldsymbol{u}}$ and $\tilde{\zeta}$ are the ADCP velocity and the relative vorticity $\zeta = \frac{\partial v}{\partial x} - \frac{\partial u}{\partial y}$ integrated similarly. Eqs. (5) & (6) were discretized using second-order-accurate, centered finite differences, which leads to the standard 5-point stencil for the Laplacian with Neumann boundary conditions. The resulting linear system of equations was solved for ψ using a fast Poisson solver based on the discrete cosine transform (Iserles 1996, Strang 1999). As shown in Fig. S3a,b for cruises 4 and 7, respectively, the solutions for ψ were almost exact in the sense that the left- and right-hand sides of Eq. (5) were nearly equal with $r^2 = 1$ and small differences between the least square fitted lines and the 1-to-1 lines.

3. RESULTS

3.1. Chl *a* below the EZ

Total chl *a* biomass in the study area above 100 m depth varied widely among cruises; the largest value of $CB_3 = 13 \times 10^5$ kg occurred during spring cruise 7 and the smallest value of 0.3×10^5 kg occurred during winter cruise 12 (Table 1). Means ± 1 SD of CB_2 and CB_3 over all cruises were similar with both at $(4.2 \pm 3.5) \times 10^5$ kg. The mean of CB_1 was $(3.0 \pm 2.5) \times 10^5$ kg. Between the repeated surveys of cruises 2, 5, 12, 14, and 15, ratios of total chl *a* biomass CB_3 (survey1/survey 2) ranged from 0.73 for cruise 2 to 4.3 for cruise 12. Fouling of the fluorometer on the profiler during survey 1 prevented comparison of biomass estimates during cruise 11.

Values of chl *a* ≥1 mg m^{-3} were observed below $p_{1\%}$ during most cruises. Spring cruise 13 had the largest $CB_{3\text{-}p1\%}$ of 3.7×10^5 kg (Table 1), and fall cruise 11 had the smallest when $CB_{3\text{-}p1\%}$ was zero. Means over all cruises of $CB_{2\text{-}p1\%}$ and $CB_{3\text{-}p1\%}$ were $(0.55 \pm 0.99) \times 10^5$ kg and $(0.60 \pm 1.09) \times 10^5$ kg, respectively, and the mean of $CB_{1\text{-}p1\%}$ was $(0.40 \pm 0.70) \times 10^5$ kg. During spring cruises 7 and 13 and winter cruise 9, more than 20% of total biomass was below $p_{1\%}$; the maximum was 35% during cruise 13. The mean fraction of chl *a* biomass below $p_{1\%}$, $CB_{3\text{-}p1\%}/CB_3$, over all cruises was 7.6 ± 9.7%. Values of $CB_{1\text{-}p1\%}/CB_1$ and $CB_{2\text{-}p1\%}/CB_2$ were similar.

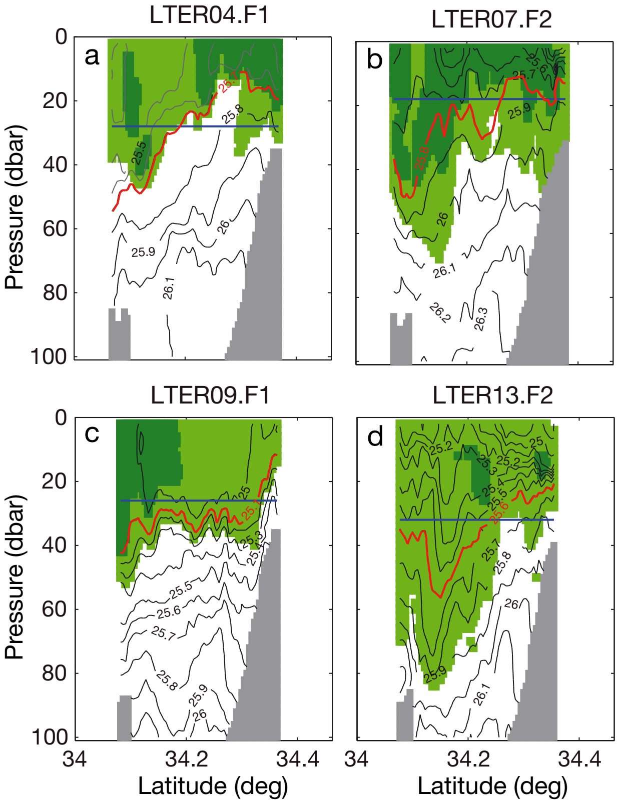

Fig. 2. Vertical sections of potential density anomaly σ_θ (solid contour lines) in kg m^{-3}, and chlorophyll *a* concentration, i.e. 1 ≤ chl *a* < 5 mg m^{-3} (light green) and chl *a* ≥5 mg m^{-3} (dark green), for line F during (a) cruise 4, (b) cruise 7, (c) cruise 9, (d) and cruise 13. Gray areas: sea floor; red lines: selected isopycnals as described in Section 3.1; horizontal blue lines: $p_{1\%}$ (pressure at the 1% light depth)

Sections of chl *a* fluorescence showed extensive areas below $p_{1\%}$ where chl *a* ≥ 1 mg m^{-3} such as along line F from cruises 4, 7, 9, and 13 (Fig. 2). For example, during cruise 13 when $p_{1\%}$ was 32 dbar, chl *a* ≥1 mg m^{-3} extended to about 80 dbar along line F (Fig. 2d). A similar pattern occurred along line F during cruise 7, when areas with chl *a* ≥1 mg m^{-3} extended to almost 70 dbar (Fig. 2b). During cruises 4 and 9, chl *a* ≥1 mg m^{-3} extended to shallower depths below $p_{1\%}$ (Fig. 2a,c).

Measurements of chl *a* from water samples also showed that high concentrations occurred below the EZ. Bottle samples below $p_{1\%}$ with chl *a* ≥1 mg m^{-3} were collected in 10 of the 13 CTD grids during cruises when towed surveys were also made. Fig. 3 shows that all chl *a* bottle samples collected during cruises 4, 7, 9, and 13 and most samples below $p_{1\%}$ had chl *a* ≥1 mg m^{-3}. These cruises had the highest percent chl *a* biomass below $p_{1\%}$ (column $CB_{3\text{-}p1\%}/CB_3$ in Table 1). Some bottle samples from spring CalCOFI cruises within or near the Santa Barbara Channel also

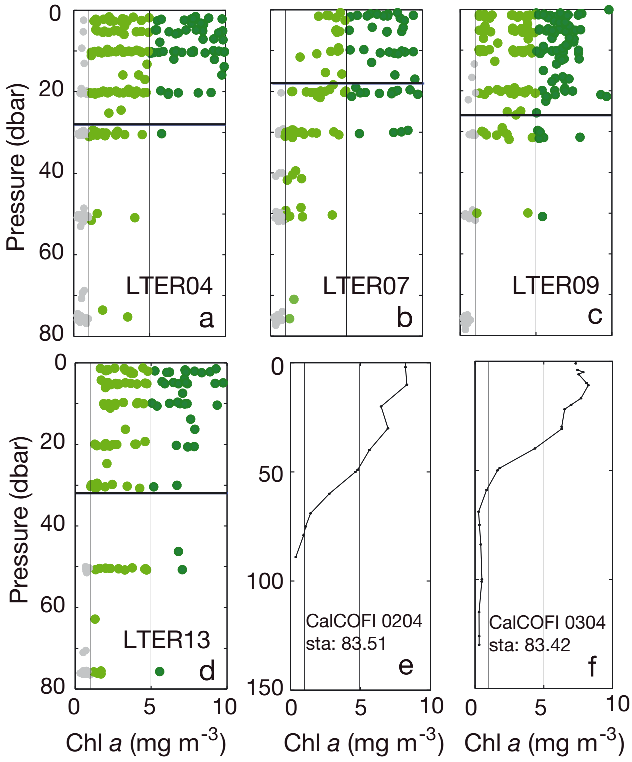

Fig. 3. Chlorophyll *a* concentration from bottle samples at all stations during (a) cruise 4, (b) cruise 7, (c) cruise 9, (d) cruise 13. Horizontal blue lines in panels (a)–(d): $p_{1\%}$ (pressure at the 1% light depth); colored circles show samples with chl *a* concentration—light gray: chl *a* <1 mg m^{-3}, light green: $1 \leq$ chl $a < 5$ mg m^{-3}, and dark green: chl $a \geq 5$ mg m^{-3}. Also shown are profiles of chl *a* from bottle samples collected during CalCOFI cruise 0204 at Stns (e) 83.51 and (f) 83.42. Vertical lines in all panels indicate chl *a* = 1 and 5 mg m^{-3}

had chl $a \geq 1$ mg m^{-3} at depths likely below the EZ ($p_{1\%}$ was not measured during the CalCOFI cruises). For example, at Station (Stn) 83.42 during CalCOFI cruise 0203 on 15 April 2003, chl $a \geq 1$ mg m^{-3} extended to 59 dbar, a pressure exceeding any $p_{1\%}$ observed during the SBC LTER cruises (Fig. 3f). At Stn 83.51 during CalCOFI cruise 0204 on 8 April 2002, chl *a* ≥ 1 mg m^{-3} extended to 75 dbar (Fig. 3e). CalCOFI station locations are shown in Fig. 1. CalCOFI cruise 0204 preceded SBC LTER cruise 4 by 18 d. CalCOFI cruise 0203 preceded SBC LTER cruise 7 by 34 d.

3.2. Subduction of phytoplankton out of the EZ

Vertical sections of chl *a* and potential density anomaly σ_θ indicated that one process transporting chl *a* below the EZ was subduction along sloping σ_θ surfaces (hereafter isopycnals). Deepening of chl *a* and σ_θ was observed during cruises 2, 4, 7, 9, and 13–16. Evidence for this is in the congruent patterns of chl *a* and isopycnals below $p_{1\%}$ in many sections from the cruises, such as along line F during cruises 4, 7, 9, and 13 (Fig. 2). Some isopycnals with chl *a* ≥ 1 mg m^{-3} in these sections could be traced upward above $p_{1\%}$ within the same sections (e.g. red lines, Fig. 2), but others could not. Some isopycnals that did not rise above $p_{1\%}$ on line F did so in other sections to the west, indicating consistent eastward deepening of isopycnals.

Examples of progressive deepening of isopycnals and chl *a* toward the east were evident during cruises 13 (Fig. 4), 4 (Fig. 5), and 7 (Fig. 6), when some isopycnals were found mostly above $p_{1\%}$ along lines A–D, but mostly below $p_{1\%}$ farther east along lines E–H. Positions of the 25.7 kg m^{-3} isopycnal (units dropped hereafter) during cruises 13 and 4, and positions of the 25.8 isopycnal during cruise 7, along lines A, C, E, and G illustrate this eastward deepening (red lines, Figs. 4–6, respectively).

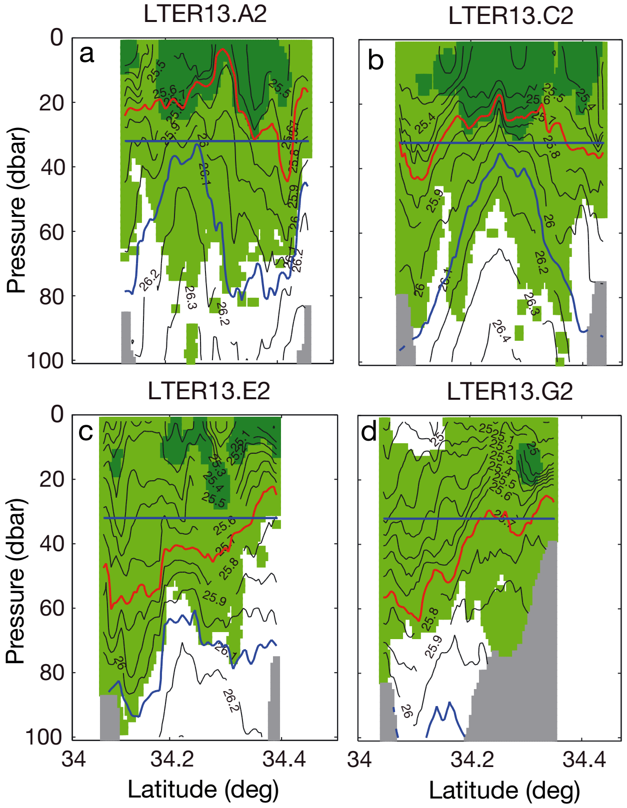

Fig. 4. Vertical sections of potential density anomaly σ_θ (solid contour lines) in kg m^{-3}, and chlorophyll *a* concentration, i.e. $1.3 \leq$ chl $a < 5$ mg m^{-3} (light green) and chl $a \geq 5$ mg m^{-3} (dark green), for cruise 13 along (a) line A, (b) line C, (c) line E, and (d) line G. Gray areas: sea floor; red lines: σ_θ = 25.7 kg m^{-3}; curving blue lines: σ_θ = 26.1 kg m^{-3}; horizontal blue lines: $p_{1\%}$ (pressure at the 1% light depth)

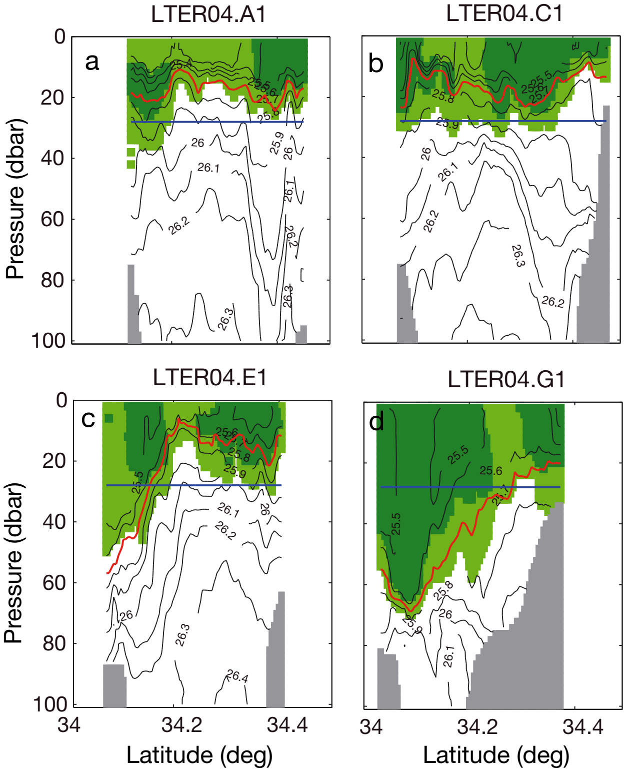

Fig. 5. As in Fig. 4, but for cruise 4. Red lines indicate σ_θ = 25.7 kg m^{-3}

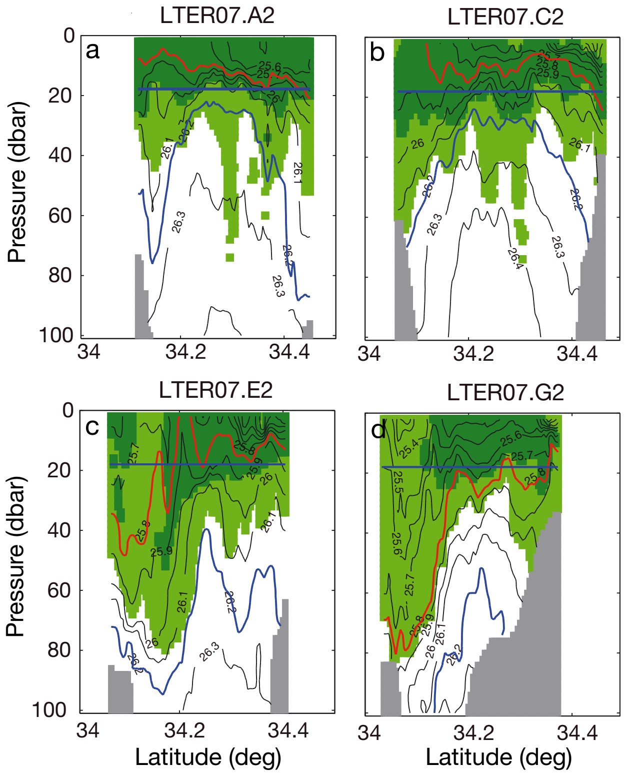

Fig. 6. As in Fig. 4, but for cruise 7. Red lines indicate σ_θ = 25.8 kg m^{-3} and blue curved lines indicate σ_θ = 26.2 kg m^{-3}

During cruise 4 along lines A and C, the 25.7 isopycnal occurred above $p_{1\%}$ everywhere, but it deepened below $p_{1\%}$ to 50 dbar in southern line E and to about 70 dbar in southern line G (Fig. 5). Comparable depth variations of the 25.7 isopycnal and chl *a* were observed along lines B, D, F, and H (not shown). The bottoms of the chl *a* patterns during cruise 4 roughly paralleled positions of the 25.7 isopycnal. Low-salinity water also progressively deepened to the east similarly to chl *a* (Fig. 7). Along the southern ends of lines A and C, S ≤33.82 occurred mostly above $p_{1\%}$, but extended below $p_{1\%}$ to about 50 dbar on line E and about 70 dbar on line G.

Similar deepening of chl *a*, S, and σ_θ was observed during cruise 7 when the 25.8 isopycnal was almost entirely above $p_{1\%}$ along lines A and C, but largely below $p_{1\%}$ along lines E and G (Fig. 6). Low-salinity water (S ≤ 33.84) paralleled the eastward descent of the 25.8 isopycnal and chl *a* below $p_{1\%}$ (Fig. 8). At the southern end of line E, S ≤33.84 was found to depths of about 53 m; S ≤33.84 was found to about 84 m on the southern end of line G (Fig. 8) and at about 88 m

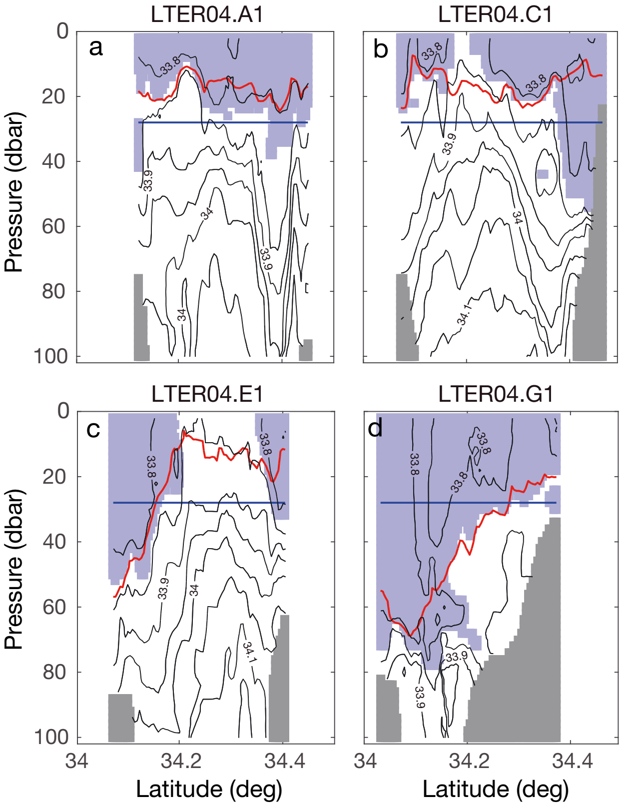

Fig. 7. Contours of salinity (S, solid contour lines) during cruise 4 along (a) line A, (b) line C, (c) line E, and (d) line G. Blue areas: S ≤33.82; gray areas: sea floor; red lines: σ_θ = 25.7 kg m^{-3}; horizontal blue lines: $p_{1\%}$ (pressure at the 1% light depth)

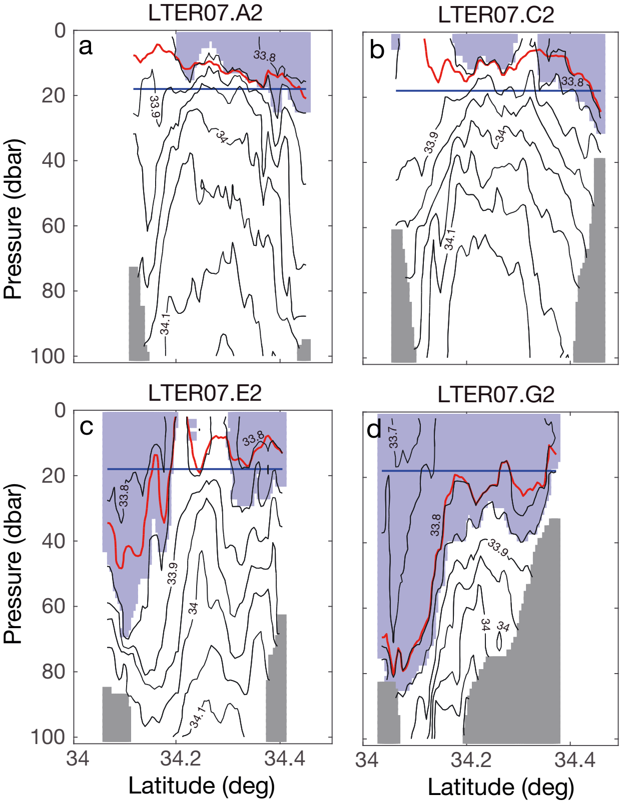

Fig. 8. As in Fig. 7, but for cruise 7. Blue areas indicate S ≤33.84. Red lines indicate σ_θ =25.8 kg m^{-3}

on the southern end of line H (not shown). The chl *a* transported below $p_{1\%}$ as indicated by congruent patterns of chl *a* and density contours mainly occurred in the southern sections of lines E–H. This was also where density in the upper 100 m decreased to the east across fronts where cooler, upwelled waters from the west met warmer waters from the east, likely from the Southern California Counter Current. We chose cruises 4 and 7 to examine the fronts in more detail because these cruises had among the highest fractions of chl *a* below $p_{1\%}$ for which shipboard ADCP data were available (Table 1).

During cruise 4, a strong front in T, S, and σ_θ extended northeastward from the channel between Santa Cruz and Santa Rosa Islands (Fig. 9a,c,d). Farther to the east and northeast, the front broadened to form a region of weaker horizontal gradients. S decreased eastward across the front from 33.96 to 33.80, while T increased from 10.2 to 12.5°C (Fig. 9a,d). Fig. 9 shows water properties at 40 dbar, but the front extended vertically from about 20 dbar to at least 100 dbar (data not shown). Above 20 dbar, the front weakened and was absent at 4 dbar (data not shown). The distribution of chl *a* ≥1 mg m^{-3} at 40 m extended across the front along sections of lines E, F, G, and H (Figs. 5c,d, & 9b) and coincided with the warmer, lower-salinity water mass (Fig. 9a,d) whose properties were similar to properties above $p_{1\%}$ west of the front.

A similar front occurred during cruise 7 when S decreased eastward across the front from 34.02 to 33.82. and T increased from 10.0 to 11.2°C at 40 dbar (Fig. 10). In contrast to cruise 4, the front extended upward to 4 dbar (data not shown), although it was weaker there than at depth. The cooler temperatures during cruise 7 compared with cruise 4 (Fig. 10a vs. Fig. 9a) may have resulted from the higher upwelling-favorable wind stress in the region (Table 1). The distribution of chl *a* ≥1 mg m^{-3} at 40 m (Fig. 10b) was more broadly distributed during cruise 7 compared with cruise 4, but a similar warmer, lower-salinity water mass coincided with the high chl *a* in the eastern channel. The T-S properties of this water mass were similar to those near the surface west of the front.

During cruises 4 and 7, ADCP velocities were generally eastward to the north of San Miguel and Santa Rosa Islands along the southern ends of lines A–D (Figs. 9c & 10c) and westward along the northern sections of lines B–E for cruise 4 and A–E for cruise 7. These are similar to frequently occurring patterns in the SBC (Harms & Winant 1998). Farther east at the fronts, ADCP velocity vectors turned cyclonically to the northeast on line E and flowed approximately parallel to the fronts. Geostrophic velocities computed from Eqs. (2) & (3) were also approximately parallel to ADCP velocities at 40 dbar in the southern sections of lines C, D, and E (Fig. 11).

Sloping isopycnals along which subduction occurred were consistent with geostrophic flow. For example, vertical sections of *u* measured by the ADCP and *u* derived from density along line C during cruise 7 were similar, indicating that conditions of geostrophic flow and thermal wind balance, as in Eqs. (2) & (3), were approximately satisfied (Fig. S4). During cruise 4, isopycnals sloped downward to the south on the southern sections of lines C–E, where *u* was mainly eastward (Figs. 5 & 12). Chl *a* ≥1 mg m^{-3} extended below $p_{1\%}$ along the 25.7 isopycnal on lines E and F south of 34.2° N (Fig. 12c,d) and farther east on lines G (Fig. 5d) and H (not shown). Patterns were reversed on the northern ends of lines C–E where isopycnals sloped downward to the north and *u* was westward, although there was no corresponding chl *a* pattern below $p_{1\%}$ (Fig. 5b,c). Similar patterns of sloping isopycnals and *u* were found during cruise 7 on lines A–E, where chl *a* ≥1 mg m^{-3} extended below $p_{1\%}$ along the 26.1 isopycnal (Figs. 6 & 13). Sub-

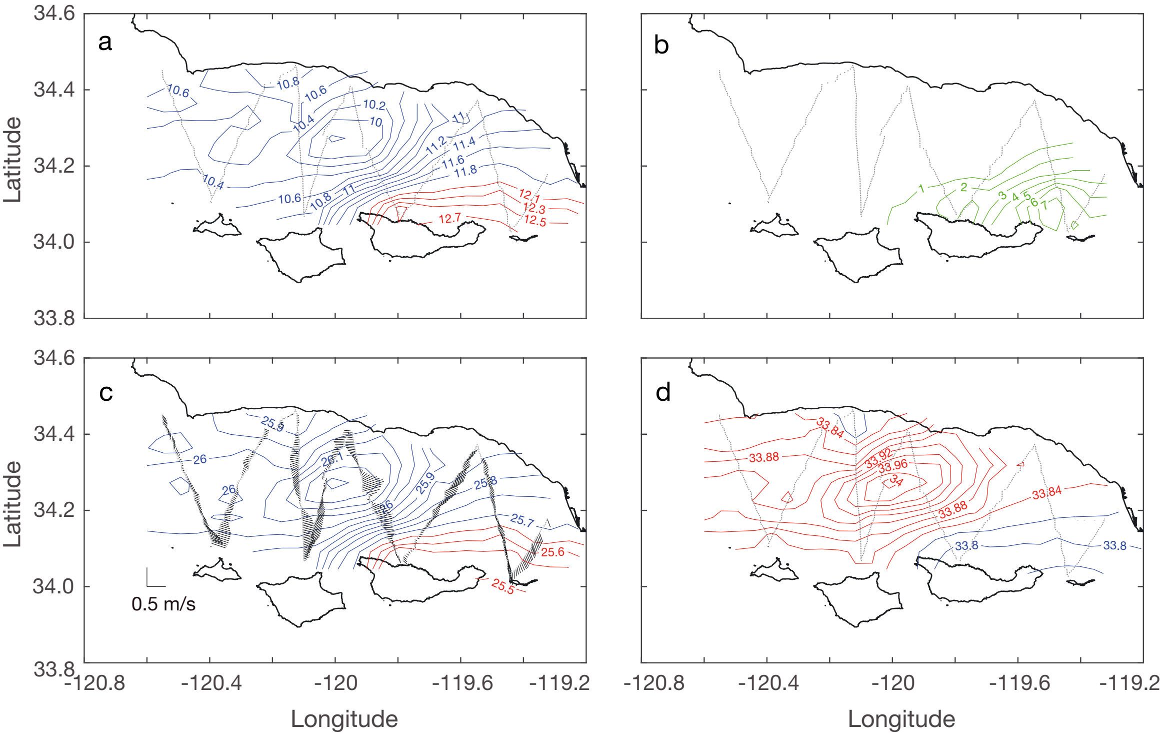

Fig. 9. Horizontal sections at p = 40 dbar during cruise 4 of (a) potential temperature, T (red contours indicate T ≥ 12.1°C; blue contours indicate T < 12.1°C); (b) chlorophyll *a* concentration (green contours indicate chl *a* = 1, 2, 3, 4, 5, 6, and 7 mg m^{-3}); (c) potential density anomaly, σ_θ (blue contours indicate $\sigma_\theta \geq 25.70$ kg m^{-3}, red contours indicate $\sigma_\theta < 25.70$ kg m^{-3}); (d) Salinity, S (red contours indicate S ≥33.84; blue contours indicate S ≤33.82). Zig-zag dotted lines in all panels show the cruise track. Short, straight black lines along cruise track in panel (c) indicate acoustic Doppler current profiler (ADCP) current vectors along the cruise track. Velocity scale shows ADCP current vectors of 0.5 m s^{-1}

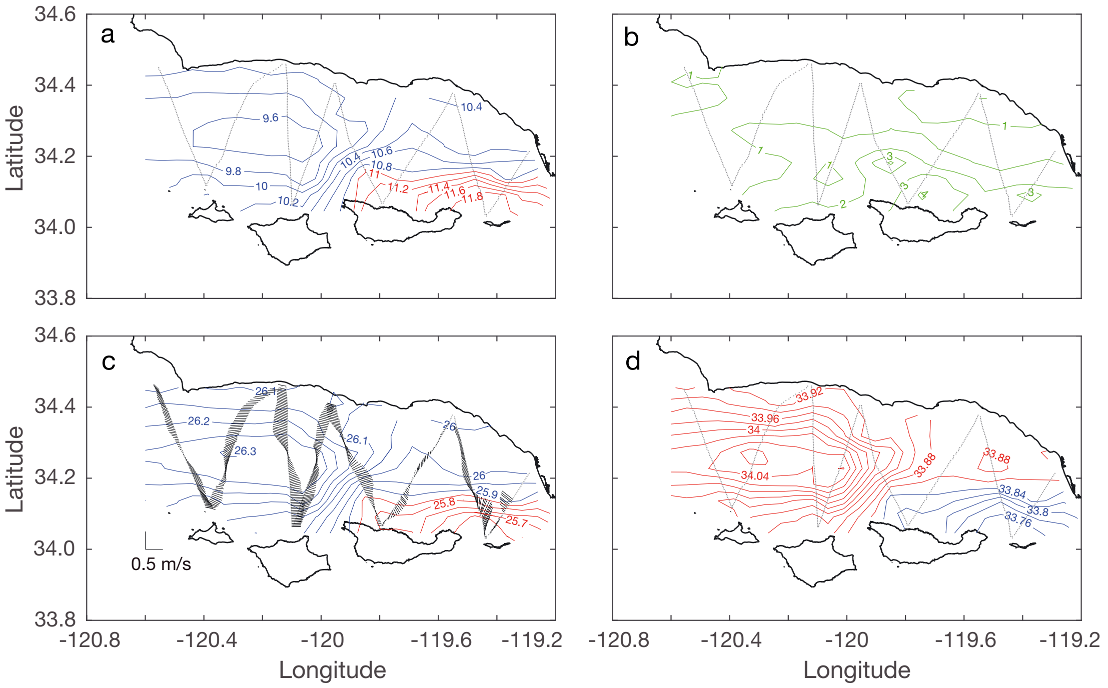

Fig. 10. Horizontal sections at p = 40 dbar during cruise 7 of (a) potential temperature, T (red contours indicate T ≥ 11.0°C; blue contours indicate T < 11.0°C); (b) chlorophyll *a* concentration (green contours indicate chl *a* = 1, 2, and 3 mg m^{-3}); (c) potential density anomaly, σ_θ (blue contours indicate $\sigma_\theta \geq 25.90$ kg m^{-3}, red contours indicate $\sigma_\theta < 25.90$ kg m^{-3}); (d) Salinity, S (red contours indicate S ≥ 33.86; blue contours indicate S ≤ 33.84) . Zig-zag dotted lines in all panels show the cruise track. Short, straight black lines along cruise track in panel (c) indicate ADCP current vectors along cruise track. Velocity scale shows ADCP current vectors of 0.5 m s^{-1}

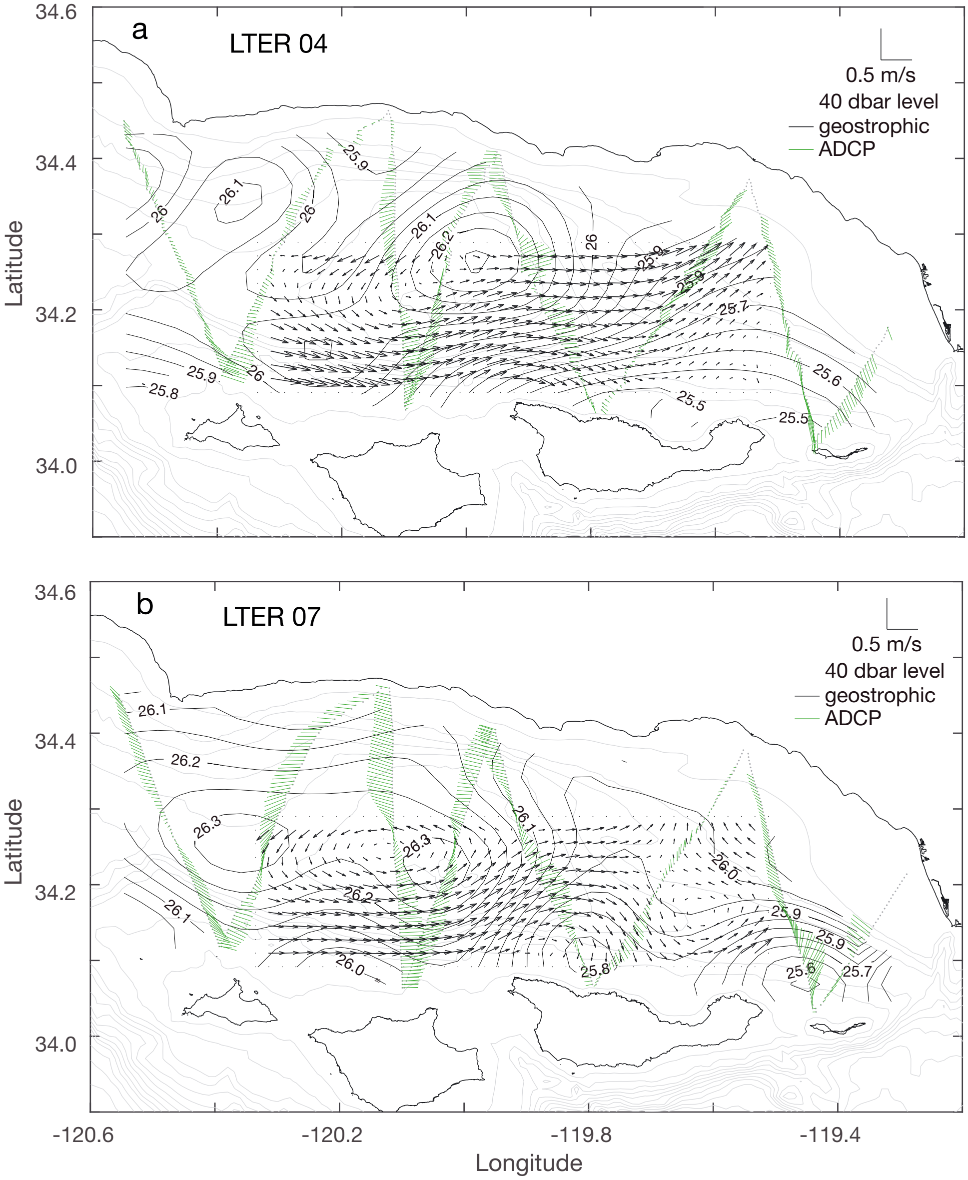

Fig. 11. Horizontal sections of ADCP velocity (u, v, short, straight green lines) and geostrophic velocity (u_g, v_g, black arrows). Velocity scale in upper right corner of each panel shows ADCP and geostrophic current vectors of 0.5 m s^{-1}. Gray dots at bases of ADCP sticks show the cruise tracks. Black contours show potential density anomaly σ_θ. Gray contours show bathymetry as in Fig. 1

ducted chl $a \geq 1$ mg m^{-3} occurred in areas of eastward u in the southern halves of lines A–E and in areas of westward u in the northern halves of those lines. Short-wavelength oscillations in the depths of isopycnals during both cruises may have resulted from internal waves.

Nutrient data from bottle samples during cruises 4, 7, and 13 provide further evidence that subduction transported chl a below the EZ. For example, subduction can explain the high chl a (= 5.6 mg m^{-3}) at 75 dbar at Stn 17 from cruise 13 (Fig. 14c). Here, σ_θ was 25.74 and the surrounding 25.7 and 25.8 isopycnals occurred mostly above $p_{1\%}$ to the west on lines A and C (Fig. 4a,b). Low nitrate + nitrite (NO_2+NO_3, hereafter nitrate) at Stn 17 was also consistent with subduction from above $p_{1\%}$ (Fig. 15c); silicate and ortho-phosphate exhibited negative anomalies at this and other stations during cruises 4, 7, and 13 where nitrate was low (data not shown). At Stn 19, where chl a >0.8 mg m^{-3}, σ_θ was less than 26.0 (Fig. 15f), but a low nitrate anomaly was less clear. Similar patterns of σ_θ and nitrate at 75 dbar consistent with subduction were observed at Stns 17, 21, and 22 during cruise 4 (Fig. 15d) and at Stn 22 during

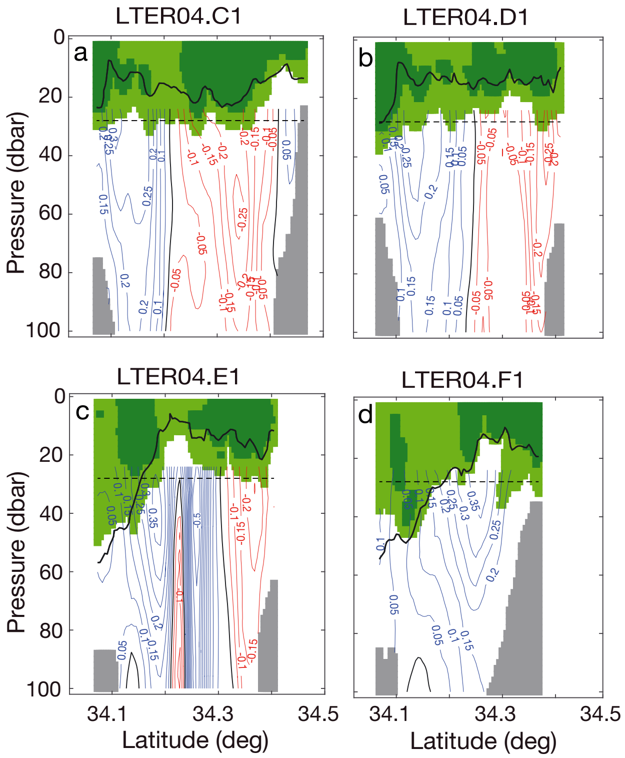

Fig. 12. Vertical sections of chlorophyll *a* concentration and contours of ADCP velocity component *u* during cruise 4 along (a) line C, (b) line D, (c) line E, and (d) line F. Green shading shows chl *a* ≥1 mg m^{-3} (light green), and chl *a* ≥5 mg m^{-3} (dark green). Blue and red contours show eastward *u* and westward *u* velocity contours, respectively, in m s^{-1}. Black lines are the zero contours of *u*. Thick black lines: σ_θ = 25.7 kg m^{-3}; gray areas: sea floor; horizontal dashed lines: $p_{1\%}$ light level

cruise 7 (Fig. 15e). Stn 16 during cruise 7 was an exception with higher σ_θ (= 26.19), but low nitrate. Subduction of previously upwelled, denser water with subsequent phytoplankton growth may explain the water properties at this station.

3.3. Gravitational sinking of phytoplankton out of the EZ

Patterns of chl *a* and salinity during cruises 1, 7, and 13 indicated that a second process transporting phytoplankton below the EZ was gravitational sinking within cyclonic flows. Chl *a* distributions during cruise 7 along lines A–D exhibited vertical bands (hereafter plumes) extending downward across isopycnals from 30 to 70 dbar between 34.2 and 34.3° N (Figs. 6 & 13). Similar plumes were observed along lines D and E during cruise 1 between 35 and 75 dbar within a similar latitude range (Fig. 16). Widths of the plumes varied from about 1 to 10 km.

Two lines of evidence support the interpretation that the plumes resulted from gravitational sinking of phytoplankton. First, the plumes extended vertically across isopycnals such that contours of chl *a* and σ_θ were not congruent in the plumes. The plumes extended below the 26.2 isopycnal in cruise 7 (Fig. 6a,b) and below the 25.98 isopycnal in cruise 1 (Fig. 16). Except for cruise 1, on line F where the 25.98 isopycnal extended above $p_{1\%}$ in a small area with chl *a* <1 mg m^{-3} (data not shown), these isopycnals were not observed above $p_{1\%}$ anywhere during their respective cruises nor were the plumes observed farther east than line D during cruise 7 and line E during cruise 1.

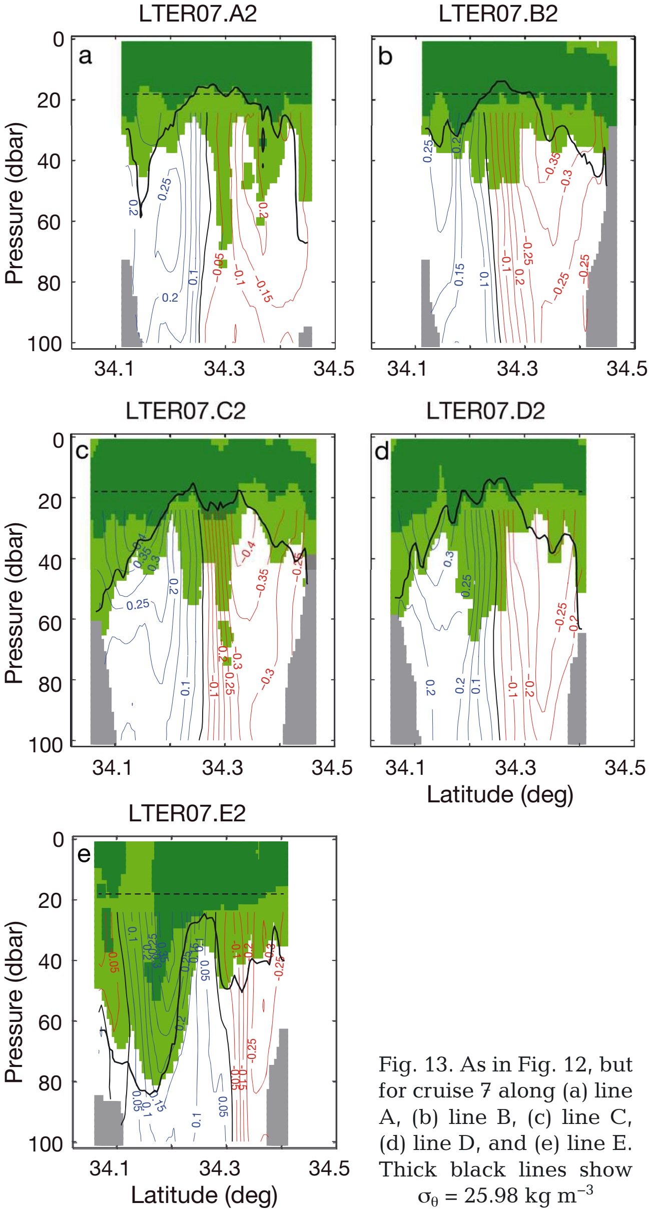

Fig. 13. As in Fig. 12, but for cruise 7 along (a) line A, (b) line B, (c) line C, (d) line D, and (e) line E. Thick black lines show σ_θ = 25.98 kg m^{-3}

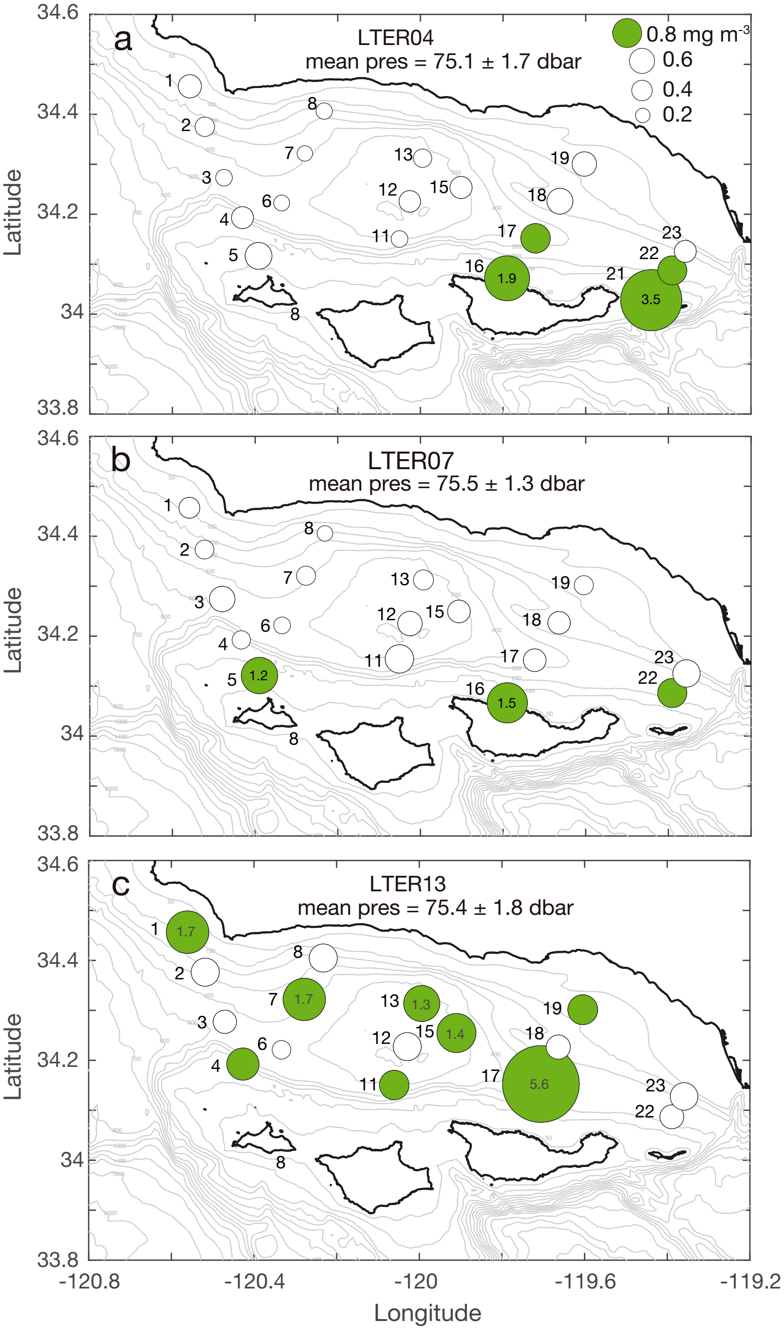

Fig. 14. Chlorophyll *a* concentration from bottle samples at a nominal depth of 75 m during (a) cruise 4, (b) cruise 7, and (c) cruise 13. Sizes of circles represent chl *a* concentration according to the scale in panel (a). Labels in larger circles show chl *a* ≥ 1 mg m^{-3}. Station numbers are given next to the circles. Statistics of sampling pressure are given in each panel. Gray lines are bathy-metric contours as in Fig. 1

Second, the patterns of low S did not parallel patterns of chl *a* within the plumes, which contrasts with patterns of S and chl *a* where water masses were subducted below $p_{1\%}$ along isopycnals. This can be seen by comparing Fig. 6a,b with Fig. 8a,b, where S ≤33.84 was mostly confined above $p_{1\%}$ while the plumes extended well below $p_{1\%}$. This is consistent with phytoplankton sinking through ambient water due to gravity, in contrast to a dissolved component like S, which does not differentially sink through ambient water due to gravity.

The plumes were found within or near regions of elevated relative vorticity during cruises 7 and 1 (Figs. 13 & 16, respectively) consistent with the presence of eddy features in the western SBC. During cruise 7, the normalized relative vorticity (hereafter vorticity) component $-{}^{\partial u}\!/_{\partial y}\, f^{-1}$ was about 0.5 around the 0 m s^{-1} isotach on lines A–D (Fig. 13). The 0 m s^{-1} isotachs were contained within or were very near the plumes (Fig. 13a–d). The vorticity distribution on lines A–D indicated near solid-body rotation where isotachs of *u* changed sign, were almost uniform vertically, and varied almost linearly in the horizontal. Much of the area of near solid-body rotation encompassed much of the plume areas. Velocities at 40 dbar revealed the presence of a cyclonic, geostrophic eddy pattern in the western side of the grid (Fig. 11b; Fig. S4). Line C crossed the center of this pattern, and plumes were observed on both sides of the zero isotach (Fig. 13c). Limited coverage of HF radar-derived surface currents also suggested a cyclonic eddy with its surface expression centered near line C (Fig. 17c). During cruise 1 along lines D and E, vertical sections showed lower *u* values with curving, less vertical isotachs, but with plumes extending well below $p_{1\%}$, including below the 25.98 isopycnal which was not found above $p_{1\%}$ on these lines (Fig. 16). The 25.98 isopycnal only rose above $p_{1\%}$ on a small section of line F (data not shown). The plumes did not coincide as closely with the zero isotachs as during cruise 7, and the vorticity component $-{}^{\partial u}\!/_{\partial y}\, f^{-1} = 0.2$ was weaker, about 0.2 on line E (Fig. 16b), and lower on line D (Fig. 16a). HF radar during cruise 1 showed a broad cyclonic flow centered near the mid-point of line D (Fig. 17a).

Similarly, cruise 13 exhibited evidence for particle sinking across isopycnals within cyclonic flow. Elevated chl *a* (≥1.3 mg m^{-3}) extended below the 26.1 isopycnal (Fig. 4b), which also showed the characteristic doming of cyclonic flow. This isopycnal was not

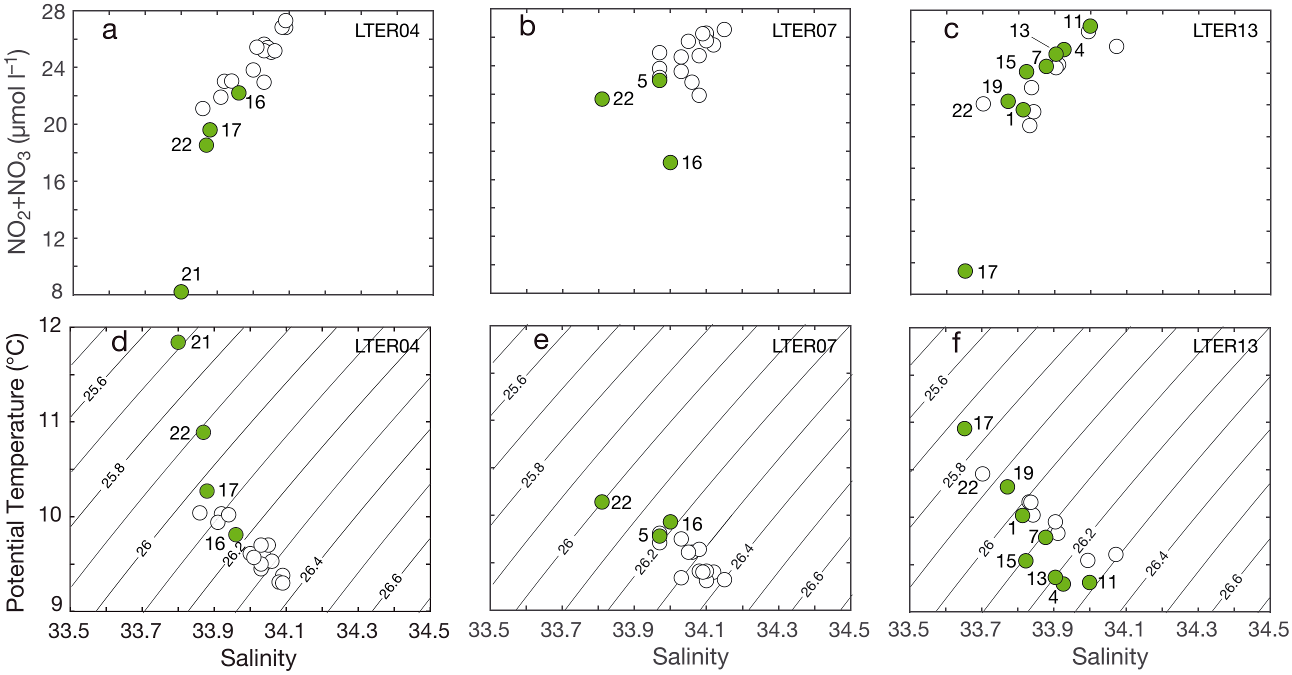

Fig. 15. Property plots of salinity versus potential temperature (lower row) and versus NO_2+NO_3 (upper row) for (a,d) cruise 4, (b,e) cruise 7, and (c,f) cruise 13. Curving lines in lower panels are potential density anomalies with values indicated by the labels. Green circles show chlorophyll *a* concentrations ≥0.8 mg m^{-3}. Station numbers are given next to the circles

found above $p_{1\%}$ anywhere in the study area. However, patterns of chl *a* and σ_θ in Fig. 4 suggested that a more complex combination of water mass subduction and gravitational sinking transported chl *a* below the EZ during cruise 13. Limited HF radar coverage showed cyclonic turning of the flow over the Santa Barbara Basin (Fig. 17d).

Chlorophyll distributions also provided evidence for gravitational sinking outside of cyclonic flows. Chl *a* from the deepest bottle samples (~75 dbar) exceeded 0.2 mg m^{-3} (detection limit, 0.01 mg m^{-3}, J. Jones pers. comm.) at all stations during cruises 4, 7, and 13, consistent with widespread sinking of phytoplankton (Fig. 14). Samples with chl *a* ≥0.8 mg m^{-3} were found away from the areas of frontal subduction, including at Stn 5 during cruise 7 (Fig. 14b) and Stns 1, 4, and 7 during cruise 13 (Fig. 16c). During cruise 13 at all but 2 stations (17 and 19) with chl *a* ≥0.8 mg m^{-3}, σ_θ exceeded 26.0 (Fig. 15f). These isopycnals occurred almost entirely below $p_{1\%}$ (Fig. 4), so the high chlorophyll concentrations were consistent with gravitational sinking of phytoplankton.

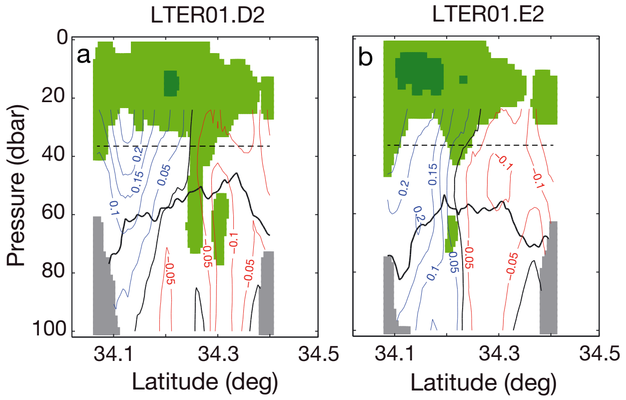

Fig. 16. As in Fig. 12, but for cruise 1 along (a) line D and (b) line E. Thick black lines show σ_θ = 25.98 kg m^{-3}

4. DISCUSSION

4.1. Chl *a* below the EZ

Measurements from the towed fluorometers and water samples from the CTD surveys support the conclusion that high chl *a* concentrations occurred below the EZ in the SBC. We argue that the presence of high chl *a* below the EZ results from a combination of subduction and particle sinking. Alternatively, increases in chl *a* at depth could arise (1) through photo-adaptation where phytoplankton increase chl *a* content under low light, and (2) through *in situ* phytoplankton growth.

Limited data were available to address photo-adaptation. Bottle samples collected within 1–2 d of

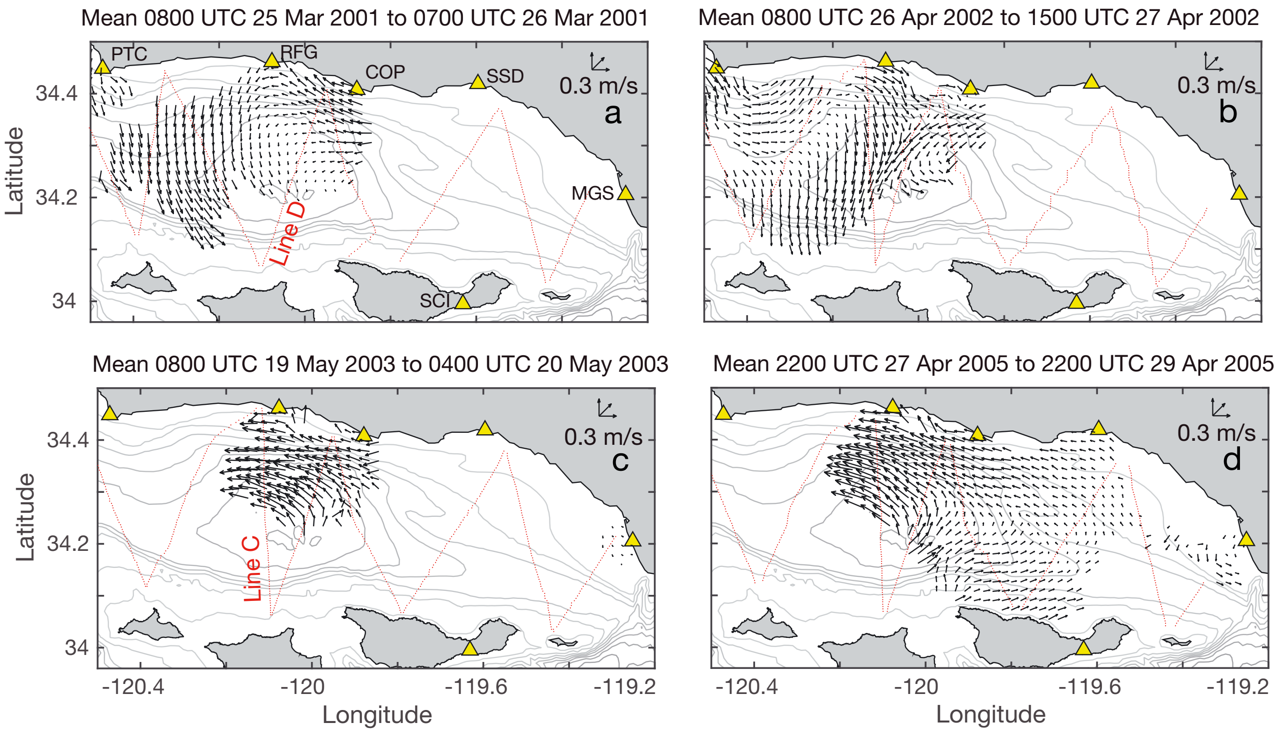

Fig. 17. Average surface currents (upper ~1 m) from high-frequency (HF) radars during towed profiler surveys for (a) cruise 1, (b) cruise 4, (c) cruise 7, and (d) cruise 13. Averaging times are given in the titles above the panels. Velocity scales in upper right corner of each panel show surface current vectors of 0.3 m s^{-1}. Lines D and C are identified in panels (a) and (c), respectively. Yellow triangles indicate HF radar sites: Point Conception (PTC), Refugio Beach (RFG), Coal Oil Point (COP), Summerland Sanitary District (SSD), Mandalay Generating Station (MGS), and Santa Cruz Island (SCI)

the towed surveys were analyzed for chl *a* and POC, and this revealed that the 2 were correlated during cruise 4 ($r^2 = 0.96$, n = 42, $p < 0.01$) and cruise 7 ($r^2 = 0.96$, n = 40, $p < 0.01$) at stations near the fronts around line E (Figs. S5 & S6). These were Stns 11, 12, 13, 15, 17, and 18, referred to as the 'front stations' in Figs. S5 & S6. Lower correlations for cruise 4 ($r^2 = 0.91$, n = 158, $p < 0.01$) and cruise 7 ($r^2 = 0.90$, n = 157, $p < 0.01$) were found based on all stations where bottle samples could be collected at pressures ≥70 dbar (Stns 1–8, 11–13, 15, 17, 18, 21–23). The high correlations between chl *a* and POC from bottle samples remained strong at values of chl *a* present below $p_{1\%}$ (generally <5 mg m^{-3}, Figs. S5 & S6). Vertical profiles of POC:chl *a* ratios (Figs. S7c & S8c) increased with pressure, which is not consistent with photo-adaptation. However, POC may comprise other carbon-containing particles besides phytoplankton (e.g. fecal pellets and detritus) that could account for this increase with pressure. These relationships provide indirect evidence that photo-adaptation was not a major driver of chl *a* below $p_{1\%}$, although it is difficult to rule out this possibility entirely based on these data.

The magnitude of *in situ* productivity below $p_{1\%}$ can be estimated based on productivity measurements reported by Brzezinski & Washburn (2011). Profiles of ^{14}C primary production were measured to the 1.7% light depth along the transect of 7 stations across the SBC on all cruises except cruises 4 and 14. As the productivity versus irradiance relationship is nearly linear at low light, those values were linearly extrapolated to the base of the EZ (1% light). Assuming that productivity ceases at the 0.1% light level, $p_{0.1\%}$ (on average 13.5 dbar below $p_{1\%}$), estimates of the depth-normalized integrated productivity between the 1 and 0.1% light levels are mathematically equivalent to half the rates at $p_{1\%}$. These correspond to a median productivity between $p_{1\%}$ and $p_{0.1\%}$ of 1.5 ± 1.4 (n = 27), 1.2 ± 0.3 (n = 28), and 0.8 ± 0.4 (n = 35) mg C m^{-3} d^{-1} during spring, fall, and winter cruises, respectively, where the uncertainty terms are median absolute deviations. We examined POC:chl *a* ratios for spring cruises 4 and 7 (Figs. S7c & S8c), and these ranged from 27 to 212 over all depths. This range of values is consistent with results of Behrenfeld et al. (2002, 2005), who compiled chl *a*:carbon ratios equivalent to ~10–1000 with a median of 100. We used a POC:chl *a* mass ratio of 30 to estimate upper bounds on median rates of chl *a* accumulation of 0.05 ± 0.05 mg m^{-3} d^{-1} (n = 27), 0.03

± 0.01 mg m^{-3} d^{-1} (n = 28), and 0.03 ± 0.01 mg m^{-3} day^{-1} (n = 35) during spring, fall, and winter, respectively. Given an average chl *a* concentration in the first 20–30 m below $p_{1\%}$ of ~2.5 mg m^{-3} (Fig. 3), it would take between 50 and 90 d to produce the observed chl *a* concentrations through biological production. These timescales exceed the residence time of about a week for near-surface waters in the SBC (Winant et al. 1999). They also exceed residence time estimates based on subsurface current speeds and the size of the SBC. Current speeds $|\boldsymbol{u}|$ at pressures within chl *a* layers below $p_{1\%}$ typically range from 0.1 to 0.2 m s^{-1} (Figs. 9–13), indicating residence times $L/|\boldsymbol{u}|$ of 5–10 d, where L = 100 km is the length of the SBC. We conclude that residence times in the SBC were too short and production below $p_{1\%}$ too low to allow much phytoplankton growth below the EZ.

4.2. Vertical transport of phytoplankton by subduction

We identified water mass subduction along sloping isopycnals as one process that transported phytoplankton below the EZ during several cruises. The sequential increase in pressure of the 25.7 isopycnal during cruise 4 illustrates how subduction developed along the southern ends of lines C–F. A sharp, 20 dbar pressure increase of the 25.7 isopycnal above $p_{1\%}$ on line C just south of 34.1° N indicated a narrow, lower-density water mass north of Santa Rosa Island (Figs. 5b & 12a). This water mass also had lower salinity (Fig. 7b). A short distance eastward, on line D, while remaining above $p_{1\%}$, this water mass had deepened and widened (Fig. 12b). Farther east on lines E and F, the 25.7 isopycnal deepened below $p_{1\%}$ to over 40 dbar and approximately paralleled the base of the subducting water mass with chl *a* ≥1 mg m^{-3} (Figs. 5c & 12c,d). The 25.7 isopycnal further deepened on lines G (Fig. 5d) and H (not shown).

As an aside, we note the pattern on line E of horizontally sheared and reversing *u* (Figs. 11a & 12c) and *v* (Fig. 11a) below 30 dbar between 34.2 and 34.3° N. We could not account for this pattern as an artifact due to changes in ship direction or ADCP malfunction. It may have been caused by an eddy about 10 km wide between the surrounding areas of larger-scale eastward and westward currents.

A similar pattern of subduction was found during cruise 7. South of 34.2° N along lines C and D, the 26.1 isopycnal approximately paralleled the bottom of the area on each line where chl *a* was ≥1 mg m^{-3}. This area deepened from a maximum of ~50 dbar on line D to ~80 dbar on E (Fig. 13d,e). Geostrophic currents flowed east–northeastward over this depth interval south of 34.25° N between lines D and E, except on the southern end of line E, where a small anticyclonic eddy-like feature produced westward flow (Figs. 11b & 13e).

Subduction of phytoplankton outside the SBC followed by transport into the channel may have also occurred. For example, during cruise 7, chl *a* ≥1 mg m^{-3} below $p_{1\%}$ at the southern ends of lines A and B coincided with current flow into the channel (Figs. 10b & 13a,b). In contrast, westward currents and chl *a* ≥1 mg m^{-3} below $p_{1\%}$ on the northern end of line A during cruise 7 illustrated a pathway for transferring subducted phytoplankton and POC from coastal waters of the northern SCB into the deeper CCS offshore.

The transport depth of subduction is limited by the isopycnal depths along which subduction occurs. During cruise 7, the maximum subduction pressure where chl a ≥1 mg m^{-3} on lines E and G was ~80 dbar (Fig. 6c,d), or about 4 times $p_{1\%}$. Corresponding subduction pressures were ~70 dbar on line F (Fig. 2b) and ~75 dbar on line H (not shown). The maximum subduction pressures approximately corresponded to the 26.1 isopycnal on line E, to the 26.0 isopycnal on line F, and to the 25.8 isopycnal on lines G and H. Density variations could have resulted from mixing of density and chl *a* before or during subduction, and internal waves could have also changed isopycnal depths. During cruise 4, the maximum subduction pressure occurred on line G at ~70 dbar, about 2.5 times $p_{1\%}$, and along the 25.7 isopycnal (Fig. 5d).

4.3. Vertical velocities and phytoplankton below the EZ

Patterns of isopycnals and horizontal currents allow rough estimates of timescales and vertical velocities of phytoplankton subduction. During cruise 4, the subducting water mass marked by the abrupt pressure increase of the 25.7 isopycnal on line D deepened by about 30 dbar between lines D and E (Fig. 12b,c). Currents were horizontally sheared within this depth interval south of 34.15° N and ranged from 0.05 to 0.2 m s^{-1}. Assuming the subducting water mass followed geostrophic current vectors along the 25.7 isopycnal over a distance of about 20 km between lines D and E (Fig. 11a), the corresponding travel times were 1–5 d and were consistent with vertical velocities of 6–30 m d^{-1}. Similar vertical velocities were estimated during cruise 7. Eastward velocities between lines D and E over the area below $p_{1\%}$ where chl *a* ≥1 mg m^{-3} ranged between 0.2 and 0.3 m s^{-1} (Fig. 13d,e). This corresponded to timescales of ~1 d and vertical velocities of ~30 m d^{-1}, again assuming isopycnal movement was along geostrophic current vectors (Fig. 11b).

Comparable vertical velocities, both upward and downward, within frontal regions of mesoscale flow structures have been diagnosed in several previous studies (Fiekas et al. 1994, Rudnick 1996, Viúdez et al. 1996a,b, Allen et al. 2001, Pallàs-Sanz et al. 2010a,b). Vertical velocities from these studies range from 8 to 90 m d^{-1} as summarized by Pallàs-Sanz et al. (2010a). Several studies have examined mesoscale eddies and semi-permanent fronts in the Alboran Sea of the Western Mediterranean, where vertical velocities ranged from 10 to 40 m d^{-1} within the fronts separating North Atlantic and Mediterranean waters (Viúdez et al. 1996b, Scott et al. 2000, Allen et al. 2001, Cutolo et al. 2022).

Studies in frontal regions of coastal waters of the CCS associated with mesoscale features such as upwelling filaments and eddies have estimated vertical velocities comparable to estimates in this study. Stukel et al. (2017) found subsurface $^{238}U/^{234}Th$ deficiencies consistent with subduction of surface waters in an eddy-related frontal region in the southern CCS. They used a data-assimilating Regional Ocean Modeling System (ROMS) model to estimate downward vertical velocities of 6–8 m d^{-1} at the core of the front. Barth et al. (2002) observed a chl *a* layer 150–250 m deep in the CCS that originated in an upwelling region near shore and then advected equatorward as it descended at ~6 m d^{-1}. In a study of a shallow frontal region within a field of mesoscale eddies and upwelling filaments in the CCS, Pallàs-Sanz et al. (2010a,b) estimated vertical velocities, both upward and downward, of 8–10 m d^{-1} that extended below 150 m depth. Kadko et al. (1991) and Washburn et al. (1991) observed chl *a* layers below the EZ in an upwelling filament in the northern CCS where deficiencies of $^{222}Rn/^{226}Ra$ and elevated oxygen concentrations indicated recent contact with the atmosphere. The depth of the layers and timescales derived from the Rn and Ra measurements were consistent with downward vertical velocities of ~25 m d^{-1}.

As shown by Freilich & Mahadevan (2019), vertical velocity can be divided into 2 components as $w = w_{uplift} + w_{iso}$, where w_{uplift} is the rate of vertical displacement of isopycnals together with tracers like chl *a* and S, and w_{iso} is the vertical component resulting from advection of tracers along sloping isopycnals. In numerical simulations of a mesoscale eddy field, they found that w_{iso} accounted for 10–25% of w. Cutolo et al. (2022) found that up to 60% of w was due to w_{iso} in a frontal region in the Alboran Sea adjacent to an anticyclonic mesoscale eddy. During cruises 4 and 7, the congruence of S and chl *a* with isopycnals and progressive deepening between lines are consistent with transport of these tracers out of the EZ by w_{iso} (Figs. 5 & 6). The large-scale tilting and arching of isopycnals during many of the cruises, including cruises 4 and 7, indicate the effects of previous w_{uplift} during formation of geostrophic eddies and eastward and westward currents. w_{uplift} also results from internal wave oscillations on shorter time and space scales.

A difference between the coastal setting of this study and the deep-ocean conditions of previous studies was the presence of nearby coastal boundaries of the Northern Channel Islands (Fig. 1). The equatorward, upwelling-favorable winds that prevailed during many of the cruises (Table 1) were downwelling-favorable along the northern coasts of the islands. Downwelling with $w_{uplift} < 0$ may explain the abrupt downward displacement of the 25.7 isopycnal (noted in Section 4.2) during cruise 4 at the southern ends of lines C and D (Fig. 12a,b) and indicate the initiation of subduction north of Santa Rosa Island.

4.4. Gravitational sinking of phytoplankton in cyclonic flows

Descending plumes of chl *a* due to gravitational sinking were found in areas of cyclonic flow exhibiting solid-body rotation during cruises 1 and 7. Limited HF radar coverage suggested that these cyclonic flows extended to the surface during cruises 1 and 7 (Fig. 17a,c), but not during cruise 4 when plumes were not observed (Fig. 17b). Cyclonic flow at the surface was also present during cruise 13 (Fig. 17d), when plumes of chl *a* were observed in regions of isopycnal uplift (Fig. 4a,b), although no ADCP data were available.

We speculate that solid-body rotation reduced shear-dispersion and horizontal mixing of the descending plumes into ambient waters. Nearly closed streamlines then isolated phytoplankton in the region of solid-body rotation over sufficiently long timescales such that gravitational sinking formed the coherent plumes. Consistent with this is the observation that the widths of the sinking plumes at times matched the widths of the areas of solid-body rotation where current velocity varied linearly with latitude (Fig. 13). During cruise 4, plumes were not observed (Fig. 5), and subsurface currents from the ADCPs (cf. Fig. 9c & 10c) and geostrophic velocities (Fig. 11) exhibited a less spatially coherent cyclonic flow pattern on lines A–E than during cruise 7.

Long residence times would also favor the accumulation of phytoplankton cells and of transparent exopolymer particles facilitating particle aggregation and sinking (Alldredge & Gotschalk 1989, Alldredge et al. 1995, Passow 2002). It is unlikely that our chl *a* observations included aggregates, as such large, rare particles would not be sampled well by the pumped fluorometers on the towed vehicles. Thus, the chl *a* signal observed beneath the regions of cyclonic flow likely came from more abundant smaller particles such as individual phytoplankton cells or chains of cells.

Numerical simulations of particle trajectories within a recurring cyclonic eddy in the western SBC support the speculation of increased residence time within the core compared with outside the eddy. Simons et al. (2015) analyzed trajectory outputs derived from the ROMS to compare 2 contrasting flow states: (1) when the eddy was persistent with stable vorticity and (2) when the eddy was intermittent with highly variable vorticity. In (1), the eddy was always present in the simulation, and the retention time within the eddy steadily increased to 25–30 d over the 70 d lifetime of the eddy. In contrast, for (2), the eddy was unstable and the retention time increased only to 9–10 d over the 35 d when the eddy could be identified.

4.5. Vertical phytoplankton transport by subduction versus gravitational sinking

By comparing temperature, salinity, and density with fluorescence-derived chl *a*, we inferred that 2 processes transported phytoplankton out of the EZ: water mass subduction at density fronts along the northern sides of the Northern Channel Islands, and gravitational sinking within cores of cyclonic eddies in the western channel. A third process, wind-driven, cross-isopycnal mixing, may have also transported chl *a* below the EZ as observed during winter cruise 9, when stratification above $p_{1\%}$ was low (Fig. 2c) and strong winds preceded the cruise (Table 1). Cross-isopycnal mixing is unlikely to account for the extensive areas of high chl *a* below the EZ, since these areas were stratified and extended across isopycnals. Vertical transport by cross-isopycnal mixing, such as occurs due to wind mixing (e.g. Fig. 2c), would tend to reduce or eliminate stratification in these areas.

Evidence for subduction was found in 7 of the 13 cruises, and evidence for particle sinking within cyclonic flows was found during 3 cruises. During cruises 7 and 13, when both processes were occurring, we estimated lower bounds on the sinking chl *a* biomass below the EZ, as the biomass found below selected isopycnals that approached, but did not rise above, $p_{1\%}$. These were regions where chl *a* had no observed connection to the EZ over which along-isopycnal transport could occur. Isopycnals selected were 26.2 for cruise 7 (Fig. 6) and 26.1 for cruise 13 (Fig. 4). For cruises 7 and 13, the fractions of chl *a* biomass below $p_{1\%}$ due to sinking were 2 and 7%, respectively.

These percentages may only represent small fractions of the total biomass of gravitationally sinking phytoplankton because: (1) chl *a* observed by the towed fluorometers probably included only small particle sizes, and not larger particles and flocs that sink rapidly (Alldredge & Gotschalk 1989, Sekula-Wood et al. 2009, Bourne et al. 2021); (2) gravitational particle sinking within subducting water masses may have contributed to the vertical transport of chl *a* biomass below the EZ, but was not separately identifiable from chl *a* fluorescence measurements alone; (3) there were areas of chl *a* above and below the selected isopycnals (Figs. 4 & 6) that resembled descending plumes of chl *a* such as during cruise 13 between 50 and 90 dbar at 34.18° N and a wider area centered on 34.35° N over a similar depth range (Fig. 4b); and (4) the presence of high chl *a* in deep (~75 m) water samples below the EZ (Fig. 14) at higher densities than those found at $p_{1\%}$ and above (Fig. 15). This indicated that gravitational sinking occurred over broader spatial scales than the cores of cyclonic eddies.

Observations were not available to quantify phytoplankton sinking rates during the LTER cruises, but previous studies indicate that the rates can be large. Alldredge & Gotschalk (1989) found that the newly formed diatom flocs had a mean sinking rate of 117 ± 56 m d^{-1} based on *in situ* measurements in the SBC. The 2 most abundant diatoms forming the flocs in their study were in the genera *Chaetoceros* and *Nitzschia*. During cruise 7, the diatom *Pseudo-nitzschia* was a dominant and toxic component of the phytoplankton assemblage (Anderson et al. 2006). Sekula-Wood et al. (2012) measured *Pseudo-nitzschia* and its toxin, domoic acid, in surface waters of the SBC and concurrently in a sediment trap at 540 m in the Santa Barbara Basin. They found significant correlations between *Pseudo-nitzschia* and domoic acid in surface waters and in the sediment trap using a 3 d lag estimated from sinking rates of Alldredge & Gotschalk (1989).

Both gravitational sinking and subduction can sustain carbon export under certain conditions. In the case of gravitational sinking, particle export can be sustained so long as carbon export is less than or equal to net primary production (NPP). This condition would be satisfied for sinking velocities ≤13 and ≤21 m d^{-1} for cruises 4 and 7, respectively, using mean NPP values of 2.2 and 5.8 gC m^{-2} d^{-1} for cruises 4 and 7, respectively (Brzezinski & Washburn 2011). Corresponding POC concentrations at the base of the EZ for cruises 4 and 7 were 0.17 and 0.28 gC m^{-3} using the least square fits for 'front' station of Figs. S5 & S6, respectively.

For subduction, suspended POC (e.g. phytoplankton) rides a conveyor consisting of lateral near-surface flows that descend beneath less dense waters at density fronts. In this case, POC export will be sustained so long as the surface flows contain significant phytoplankton biomass and subduction persists at the density fronts. We note that subduction would also export dissolved organic carbon (DOC) that has accumulated in surface waters and any upwelled dissolved inorganic carbon (DIC as CO_2) that has yet to be utilized by phytoplankton. This would further enhance carbon export due to subduction compared to particle sinking (Carlson et al. 2010). The associated carbon sequestration timescales for DOC export will be limited by the depth of subduction with eventual remineralization of much of the accumulated DOC by mesopelagic bacteria. Sinking particles, on the other hand, move vertically through the water column and may reach a greater average depth before being remineralized. This would lead to longer timescales of carbon sequestration compared to subducted particles that were suspended in the EZ prior to subduction (e.g. had low sinking rates), such that most may only travel as deep as their host water mass, <100 m (e.g. Figs. 4–6).

4.6. Summary

Our results indicate that water mass subduction at density fronts and phytoplankton sinking are important mechanisms for the vertical transport of phytoplankton and POC out of the EZ in coastal upwelling systems such as in the SBC. Phytoplankton sinking was observed as coherent plumes, but also occurred on broader horizontal scales by processes that were not resolved by our observations. Additional observations that better describe the evolution of coastal density fronts and associated vertical velocities are required to further constrain organic carbon flux due to subduction.

Data availability. Towed profiler, CTD, water sample, and shipboard underway data are available from the SBC LTER data catalog at: https://sbclter.msi.ucsb.edu/data/catalog/. All data are publicly available.

Acknowledgements. We thank the captains and crew members of the RV 'Point Sur' for their effective support during the cruises in this study; marine technicians Dave Nelson, Doug Conlin, and Stewart Lamerdin for operating the CTDs, rosettes, and towed vehicles; David Salazar and Janice Jones for providing critical technical assistance; the many graduate students, post-doctoral researchers, and volunteers who assisted during the cruises; and Nick Dellaripa, who performed the preliminary analysis of the towed profiler data. This work was supported by the US National Science Foundation's Long Term Ecological Research Program under the Division of Ocean Sciences grants OCE 9982105, OCE 0620276, OCE 1232779, OCE-1831937, and OCE 1658475.

LITERATURE CITED

Alldredge AL, Gotschalk CC (1989) Direct observations of the mass flocculation of diatom blooms: characteristics, settling velocities and formation of diatom aggregates. Deep Sea Res A 36:159–171

Alldredge A, Gotschalk CC, Passow U, Riebesell U (1995) Mass aggregation of diatom blooms: insights from a mesocosm study. Deep Sea Res II 42:9–27

Allen JT, Smeed DA, Tintoré J, Ruiz S (2001) Mesoscale subduction at the Almeria-Oran front. Part 1: Ageostrophic flow. J Mar Syst 30:263–285

Anderson CR, Brzezinski MA, Washburn L, Kudela R (2006) Circulation and environmental conditions during a toxigenic *Pseudo-nitzschia australis* bloom in the Santa Barbara Channel, California. Mar Ecol Prog Ser 327:119–133

Anderson CR, Siegel DA, Kudela RM, Brzezinski MA (2009) Empirical models of toxigenic *Pseudo-nitzschia* blooms: potential use as a remote detection tool in the Santa Barbara Channel. Harmful Algae 8:478–492

Barth JA, Cowles TJ, Kosro PM, Shearman RK, Huyer A, Smith RL (2002) Injection of carbon from the shelf to offshore beneath the euphotic zone in the California Current. J Geophys Res Oceans 107:10-1–10-8

Bassin CJ, Washburn L, Brzezinski MA, McPhee-Shaw EE (2005) Sub-mesoscale coastal eddies observed by high frequency radar: a new mechanism for delivering nutrients to kelp forests in the Southern California Bight. Geophys Res Lett 32:L12604

Beckenbach EH, Washburn L (2004) Low frequency waves in the Santa Barbara Channel observed using high frequency radar. J Geophys Res Oceans 109:C02010

Behrenfeld MJ, Marañón E, Siegel DA, Hooker SB (2002) Photoacclimation and nutrient-based model of light-saturated photosynthesis for quantifying oceanic primary production. Mar Ecol Prog Ser 228:103–117

Behrenfeld MJ, Boss E, Siegel DA, Shea DM (2005) Carbon-based ocean productivity and phytoplankton physiology from space. Global Biogeochem Cycles 19:GB1006

Bourne HL, Bishop JKB, Connors EJ, Wood TJ (2021) Carbon export and fate beneath a dynamic upwelled filament off the California coast. Biogeosciences 18: 3053–3086

Boyd PW, Claustre H, Levy M, Siegel DA, Weber T (2019) Multi-faceted particle pumps drive carbon sequestration in the ocean. Nature 568:327–335

Bray NA, Keyes A, Morawitz WML (1999) The California Current System in the Southern California Bight and the Santa Barbara Channel. J Geophys Res Oceans 104: 7695–7714

Brzezinski MA, Washburn L (2011) Phytoplankton primary productivity in the Santa Barbara Channel: effects of wind-driven upwelling and mesoscale eddies. J Geophys Res Oceans 116:C12013

Buesseler KO, Boyd PW, Black EE, Siegel DA (2020) Metrics that matter for assessing the ocean biological carbon pump. Proc Natl Acad Sci USA 117:9679–9687

Caldwell PC, Stuart DW, Brink KH (1986) Mesoscale wind variability near Point Conception, California during Spring 1983. J Clim Appl Meteorol 25:1241–1254

Carlson CA, Hansell DA, Nelson NB, Siegel DA and others (2010) Dissolved organic carbon export and subsequent remineralization in the mesopelagic and bathypelagic realms of the North Atlantic basin. Deep Sea Res II 57: 1433–1445

Checkley DM, Barth JA (2009) Patterns and processes in the California Current System. Prog Oceanogr 83:49–64

Cutolo E, Pascual A, Ruiz S, Johnston TMS and others (2022) Diagnosing frontal dynamics from observations using a variational approach. J Geophys Res Oceans 127: e2021JC018336

Dorman CE, Winant CD (2000) The structure and variability of the marine atmosphere around the Santa Barbara Channel. Mon Weather Rev 128:261–282

Evans W, Hales B, Strutton PG, Shearman RK, Barth JA (2015) Failure to bloom: Intense upwelling results in negligible phytoplankton response and prolonged CO_2 outgassing over the Oregon shelf. J Geophys Res Oceans 120:1446–1461

Fennel K, Alin S, Barbero L, Evans W and others (2019) Carbon cycling in the North American coastal ocean: a synthesis. Biogeosciences 16:1281–1304

Fiekas V, Leach H, Mirbach KJ, Woods JD (1994) Mesoscale instability and upwelling. Part 1: Observations of the North Atlantic Intergyre Front. J Phys Oceanogr 24:1750–1758

Flament P, Armi L (2000) The shear, convergence, and thermohaline structure of a front. J Phys Oceanogr 30:51–66

Fram JP, Stewart HL, Brzezinski MA, Gaylord B, Reed DC, Williams SL, MacIntyre S (2008) Physical pathways and utilization of nitrate supply to the giant kelp, *Macrocystis pyrifera.* Limnol Oceanogr 53:1589–1603

Freilich MA, Mahadevan A (2019) Decomposition of vertical velocity for nutrient transport in the upper ocean. J Phys Oceanogr 49:1561–1575

Goodman J, Brzezinski MA, Halewood ER, Carlson C (2012) Sources of phytoplankton to the inner continental shelf in the Santa Barbara Channel inferred from cross-shelf gradients in biological, physical and chemical parameters. Cont Shelf Res 48:27–39

Harms S, Winant CD (1998) Characteristic patterns of the circulation in the Santa Barbara Channel. J Geophys Res Oceans 103:3041–3065

Hickey BM (1979) The California Current System: hypotheses and facts. Prog Oceanogr 8:191–279

Hickey BM (1993) Physical oceanography. In: Dalley MD, Reish DJ, Anderson JW (eds) Ecology of the Southern California Bight. University of California Press, Berkeley, CA, p 19–70

Hickey BM (1998) Coastal oceanography of western North America from the tip of Baja California to Vancouver Island. In: Robinson AR, Brink KH (eds) The sea. John Wiley and Sons, New York, NY, p 345–393

Hood RR, Abbott MR, Huyer A (1991) Phytoplankton and photosynthetic light response in the Coastal Transition Zone off northern California in June 1987. J Geophys Res Oceans 96:14769–14780

Iserles A (1996) A first course in the numerical analysis of differential equations. Cambridge University Press, Cambridge

Kadko DC, Washburn L, Jones B (1991) Evidence of subduction within cold filaments of the Northern California Coastal Transition Zone. J Geophys Res Oceans 96: 14909–14926

Lucas AJ, Dupont CL, Tai V, Largier JL, Palenik B, Franks PJS (2011a) The green ribbon: multiscale physical control of phytoplankton productivity and community structure over a narrow continental shelf. Limnol Oceanogr 56:611–626

Lucas AJ, Franks PJS, Dupont CL (2011b) Horizontal internal-tide fluxes support elevated phytoplankton productivity over the inner continental shelf. Limnol Oceanogr Fluids Environ 1:56–74

Lynn RJ, Simpson JJ (1987) The California Current System: the seasonal variability of its physical characteristics. J Geophys Res Oceans 92:12947–12966

Mantyla AW, Venrick EL, Hayward TL (1995) Primary production and chlorophyll relationships, derived from 10 years of CalCOFI measurements. Calif Coop Ocean Fish Invest Rep 36:159–166

McPhee-Shaw EE, Siegel DA, Washburn L, Brzezinski MA, Jones JL, Leydecker A, Melak J (2007) Mechanisms for nutrient delivery to the inner shelf: observations from the Santa Barbara Channel. Limnol Oceanogr 52:1748–1766

Miller RJ, Reed DC, Brzezinski MA (2011) Partitioning of primary production among giant kelp (*Macrocystis pyrifera*), understory macroalgae, and phytoplankton on a temperate reef. Limnol Oceanogr 56:119–132

Murphy AM, Cowles TJ (1997) Effects of darkness on multi-excitation *in vivo* fluorescence and survival in a marine diatom. Limnol Oceanogr 42:1444–1453

Nishimoto MM, Washburn L (2002) Patterns of coastal eddy circulation and abundance of pelagic juvenile fish in the Santa Barbara Channel, California, USA. Mar Ecol Prog Ser 241:183–199

Oey LY, Wang DP, Hayward T, Winant C (2001) 'Upwelling' and 'cyclonic' regimes of the near-surface circulation of the Santa Barbara Channel. J Geophys Res Oceans 106: 9213–9222

Otero MP, Siegel DA (2004) Spatial and temporal characteristics of sediment plumes and phytoplankton blooms in the Santa Barbara Channel. Deep Sea Res II 51:1129–1149

Pallàs-Sanz E, Johnston TMS, Rudnick DL (2010a) Frontal dynamics in a California Current System shallow front: 2. Mesoscale vertical velocity. J Geophys Res Oceans 115: C12068

Pallàs-Sanz E, Johnston TMS, Rudnick DL (2010b) Frontal dynamics in a California Current System shallow front: 1. Frontal processes and tracer structure. J Geophys Res Oceans 115:C12067

Passow U (2002) Transparent exopolymer particles (TEP) in aquatic environments. Prog Oceanogr 55:287–333

Rudnick DL (1996) Intensive surveys of the Azores front: 2. Inferring the geostrophic and vertical velocity fields. J Geophys Res Oceans 101:16291–16303

Schiff K, Greenstein D, Dodder N, Gillett DJ (2016) Southern California Bight regional monitoring. Reg Stud Mar Sci 4:34–46

Scott RK, Allen JS, Egbert GD, Miller RN (2000) Assimilation of surface current measurements in a coastal ocean model. J Phys Oceanogr 30:2359–2378

Sekula-Wood E, Schnetzer A, Benitez-Nelson CR, Anderson C and others (2009) Rapid downward transport of the neurotoxin domoic acid in coastal waters. Nat Geosci 2:272–275

Sekula-Wood E, Benitez-Nelson C, Morton S, Anderson C, Burrell C, Thunell R (2011) *Pseudo-nitzschia* and domoic acid fluxes in Santa Barbara Basin (CA) from 1993 to 2008. Harmful Algae 10:567–575

Sekula-Wood E, Benitez-Nelson CR, Bennett M, Thunell R (2012) Magnitude and composition of sinking particulate phosphorus fluxes in Santa Barbara Basin, California. Global Biogeochem Cycles 26:GB2023

Selkoe KA, Gaines SD, Caselle JE, Warner RR (2006) Current shifts and kin aggregation explain genetic patchiness in fish recruits. Ecology 87:3082–3094

Shipe RF, Brzezinski MA (2001) A time series study of silica production and flux in an eastern boundary region: Santa Barbara Basin, California. Global Biogeochem Cycles 15:517–531

Shipe RF, Passow U, Brzezinski MA, Graham W, Pak D, Siegel DA, Alldredge AA (2002) Effects of the 1997–98 El Niño on seasonal variations in suspended and sinking particles in the Santa Barbara basin. Prog Oceanogr 54: 105–127

Simons RD, Nishimoto MM, Washburn L, Brown KS, Siegel DA (2015) Linking kinematic characteristics and high concentrations of small pelagic fish in a coastal meso scale eddy. Deep Sea Res I 100:34–47

Soutar A, Crill PA (1977) Sedimentation and climatic patterns in the Santa Barbara Basin during the 19th and 20th centuries. Geol Soc Am Bull 88:1161–1172

Soutar A, Kling SA, Crill PA, Duffrin E, Bruland KW (1977) Monitoring the marine environment through sedimentation. Nature 266:136–139

Strang G (1999) The discrete cosine transform. SIAM Rev 41:135–147

Stukel MR, Aluwihare LI, Barbeau KA, Chekalyuk A and others (2017) Mesoscale ocean fronts enhance carbon export due to gravitational sinking and subduction. Proc Natl Acad Sci USA 114:1252–1257

Stukel MR, Song H, Goericke R, Miller AJ (2018) The role of subduction and gravitational sinking in particle export, carbon sequestration, and the remineralization length scale in the California Current Ecosystem. Limnol Oceanogr 63:363–383

Thunell RC (1998) Particle fluxes in a coastal upwelling zone: sediment trap results from Santa Barbara Basin, California. Deep Sea Res II 45:1863–1884

Thunell RC, Tappa E, Anderson DM (1995) Sediment fluxes and varve formation in Santa Barbara Basin, offshore. Calif Geol 23:1083–1086

Viúdez Á, Haney RL, Tintoré J (1996a) Circulation in the Alboran Sea as determined by quasi-synoptic hydrographic observations. Part II: Mesoscale ageostrophic motion diagnosed through density dynamical assimilation. J Phys Oceanogr 26:706–724

Viúdez A, Tintoré J, Haney R (1996b) Circulation in the Alboran Sea as determined by quasi-synoptic hydrographic observations. Part I: Three-dimensional structure of the two anticyclonic gyres. J Phys Oceanogr 26:684–705

Washburn L, Kadko DC, Jones BH, Hayward T and others (1991) Water mass subduction and the transport of phytoplankton in a coastal upwelling system. J Geophys Res Oceans 96:14927–14945

Winant CD, Alden DJ, Dever EP, Edwards KA, Hendershott MC (1999) Near-surface trajectories off central and southern California. J Geophys Res Oceans 104: 15713–15726

Winant CD, Dever EP, Henderschott MC (2003) Characteristic patterns of shelf circulation at the boundary between central and southern California. J Geophys Res Oceans 108:3021

Editorial responsibility: Katherine Richardson, Copenhagen, Denmark
Reviewed by: 2 anonymous referees, and previous version reviewed in MEPS by 3 anonymous referees

Submitted: April 16, 2022
Accepted: July 28, 2023
Proofs received from author(s): September 8, 2023